

Alpha-particle confinement in Infinity Two Fusion Pilot Plant baseline plasma design

L. Carbajal^{1†}, J. Varela¹, A. Bader¹, W. Guttenfelder¹, A. Cerfon¹, J. C. Schmitt¹, J. Morrissey¹, C. C. Hegna¹, J. M. Canik¹, N. R. Mandell¹, M. Landreman¹, K. Willis¹, D. Huet¹, D. Clark¹, K. Camacho Mata¹, N. M. Davila¹, W. A. Cooper^{1,2}, W. D. Dorland¹, J. M. Duff¹, G. Le Bars¹, A. Malkus¹, L. Singh¹, B. Medasani¹, P. Sinha¹, K. Särkimäki³, J. Sissonen³, A. Snicker³,

¹Type One Energy, Knoxville, TN, 37931, USA

²Swiss Alps Fusion Energy (SAFE), Vers l'Eglise, Switzerland

³VTI Technical Research Centre of Finland Ltd, Espoo, Finland

In this work, we present a detailed assessment of fusion-born alpha-particle confinement, their wall loads, and stability of Alfvén eigenmodes driven by these energetic particles in the Infinity Two Fusion Pilot Plant Baseline Plasma Design, a 4-field-period quasi-isodynamic stellarator to operate in deuterium-tritium fusion conditions. Using the Monte-Carlo codes SIMPLE, ASCOT5, and KORC-T, we study the collisionless and collisional dynamics of guiding-center and full-orbit alpha-particles in the core plasma. We find that core energy losses to the wall are less than 4%. Our simulations show that peak power loads on the wall of this configuration are around 2.5 MW/m² and are spatially localized, toroidally, and poloidally in the vicinity of x-points of the magnetic island chain $n/m = 4/5$ outside the plasma volume. Also, an exploratory analysis using various simplified walls shows that shaping and distance of the wall from the plasma volume can help reduce peak power loads. Our stability assessment of Alfvén eigenmodes using the STELLGAP and FAR3d codes shows the absence of unstable modes driven by alpha-particles in Infinity Two due to the relatively low alpha-particle beta at the envisioned 800 MW operating scenario.

1. Introduction

Fusion pilot plants (FPP) using deuterium-tritium (DT) plasmas as fuel rely on achieving good fusion-born alpha-particle confinement for providing plasma heating to maintain plasma burning conditions (Warmer *et al.* 2016; Alonso *et al.* 2022; Prost & Volpe 2023) and to avoid damage to plasma facing components due to constant bombardment by these very energetic ions (Mau *et al.* 2008; El-Guebaly 2018). Energetic ion confinement is a central driver in optimized stellarator design due to the challenge of finding three-dimensional magnetic fields that provide robust confinement of these particles. However, considerable progress has been made in this area in recent years with the advent of new theoretical tools to address alpha particle orbits in 3D configurations as well as new methods to improve energetic ion confinement in optimization (Nemov *et al.* 2008; Bader *et al.* 2019; Velasco *et al.* 2021; Paul *et al.* 2022). The primary goal of this study is to demonstrate that modern optimization techniques can be used to produce stellarator FPP designs that meet the requirements needed from energetic ion confinement as embodied

† Email address for correspondence: leo.carbajal@typeoneenergy.com

in the Infinity Two baseline plasma physics design (Hegna *et al.* 2025). Infinity Two is a four-field period, aspect ratio $A = 10$, quasi-isodynamic configuration with improved confinement appealing to three-dimensional shape optimization, elevated plasma density and high magnetic field ($B = 9T$). Excellent energetic ion confinement is an explicit goal of the Infinity Two design.

Alpha particle confinement will be the emphasis of the following study. Other densities of fusion-born ions, and their corresponding plasma heating, produced in primary fusion reactions in DT plasmas such as 1.01 MeV tritium, 3.02 MeV protons, and 0.82 MeV He^3 , are expected to be much lower than fusion-born 3.5 MeV alpha-particles (Lazerson *et al.* 2021*b*); therefore, we only focus on the latter in this work.

Most current tokamaks and stellarators/heliotrons can study the dynamics of fast ions through the introduction of auxiliary heating systems such as radio frequency (RF) heating and neutral beam injection (NBI). Current experiments studying fast-ion dynamics can provide valuable insights into the loss mechanisms of alpha-particles in future fusion reactors. In the stellarator W7-X, the dynamics of fast ions produced by RF and NBI have been analyzed via interpretative modeling using guiding-center (GC) and full-orbit (FO) Monte-Carlo codes such as BEAMS3D, ASCOT5, and VENUS-LEVIS. These simulations have been compared against experimental measurements of wall loads of fast ions (Äkäslompolo *et al.* 2018; Lazerson *et al.* 2021*a,c*, 2023, 2024). In these studies it is consistently found that trapped fast ions dominate prompt losses. Prompt losses are fast ions that quickly leave the plasma before they slow-down, and therefore provide minimal heating of the plasma while causing damage to machine components. When comparing guiding-center estimates of fast-ion losses against full-orbit estimates, it is found that the latter are always higher (Lazerson *et al.* 2024). Additionally, a study of fast-ion losses in the presence of magnetic islands at the core of W7-X has been done, showing degradation of fast-ion confinement with increasing size of core magnetic islands (Lazerson *et al.* 2024).

Similarly, in LHD plasmas, fast-ions are routinely produced by RF and NBI and simulated using GC and FO Monte-Carlo codes (Krasilnikov *et al.* 2002; Ogawa *et al.* 2013, 2024). As in W7-X plasmas, it is found that trapped fast-ions are more likely to get lost. Of particular interest are the studies of fast-ion dynamics in LHD showing robust fast-ion confinement in the presence of sawtooth-like activity (Moseev *et al.* 2024), and degradation of fast-ion confinement in the presence of toroidal Alfvén eigenmodes (TAE) with increasing TAE amplitudes (Ogawa *et al.* 2013).

Alfvén eigenmodes (AE) are plasma waves supported by the thermal plasma that can be destabilized by fusion-born ions in fusion reactors and subsequently provided enhanced fusion-born ion losses. AE have been extensively studied in the past (Heidbrink 2008). Experimental confirmation of fusion-born alpha-particles destabilization of Toroidal Alfvén eigenmodes (TAE) in the latest JET DT plasmas was found (Fitzgerald *et al.* 2023). Detailed analysis of TAE activity in LHD has been performed (Ogawa *et al.* 2010; Spong *et al.* 2010), showing a more complex structure of modes than that of tokamaks due to the more complex magnetic field structure of helical devices. For these analysis, stability codes including the 3D structure of stellarator plasmas such as AE3D (Spong *et al.* 2003), STELLGAP (Spong *et al.* 2010), and FAR3d (Varela *et al.* 2024*d*) have been used.

Fast ions created by RF and neutral beams are relatively low-energy (tens to few hundreds of keV) with respect to fusion-born 3.5 MeV alpha-particles, and mainly interact with the background ions via collisions. In contrast, fusion-born alpha-particles interact more strongly with background electrons. Fast ions from RF and NBI mainly heat background ions while fusion-born alpha-particles mainly heat electrons. Also, fast

ions in the tens of keV range might be more strongly influenced by electric fields in the plasma, while for alpha-particles these effects are much less relevant. Only in DT plasmas of the tokamak experiments TFTR and JET has it been possible to directly study fusion-born alpha-particle dynamics, and evidence of alpha-heating of electrons has been observed (Hawryluk *et al.* 1994; Kiptily *et al.* 2023).

Recent advancements in methods for designing and optimizing stellarator power plants (Landreman *et al.* 2022; Sánchez *et al.* 2023; Goodman *et al.* 2024) make it possible to achieve attractive confinement of fusion-born alpha-particles along with all other desired properties for a stellarator FPP. In Refs. (Bader *et al.* 2021; Velasco *et al.* 2021; Paul *et al.* 2022, 2023; Sánchez *et al.* 2023), the authors have performed a detailed analysis of alpha-particle confinement in optimized reactor-scale stellarators. It is found that, in agreement with experimental measurements and interpretative simulations of fast ions in existing devices, trapped alpha-particles dominate prompt losses in the studied devices. However, techniques have been developed in the stellarator optimization community to overcome these losses.

In this work, we present a detailed analysis of fusion-born alpha-particle dynamics in Type One Energy optimized stellarator, Infinity Two Fusion Pilot Plant Baseline Plasma Design (Hegna *et al.* 2025). Energetic ion confinement was one of the major objectives in the optimization strategy used to generate favorable configurations. The baseline Infinity Two design is a quasi-isodynamic (QI) stellarator whose good confinement is sought by seeking the alignment of the second adiabatic invariant $J = \int mv_{\parallel} dl$ with the flux surfaces. Additionally, Infinity Two was optimized by attempting to align both B_{min} and B_{max} values along the field line. That is, $B_{min}(B_{max})$ has a common value of the local minima (maxima) of B along the field line. Alignment of local extrema (especially local minima) tends to be important for energetic particle confinement as well. Using a set of state-of-the-art codes, we show that good alpha-particle confinement and manageable wall loads can both be achieved in this device.

We use the SIMPLE, ASCOT5, and KORC-T Monte-Carlo codes to simulate collisionless and collisional guiding-center (GC) and full-orbit (FO) simulations of fusion-born ions in Infinity Two. We use the SIMPLE code (Albert *et al.* 2020) to perform collisionless GC simulations of alpha-particles in a free-boundary VMEC equilibrium (Hirshman *et al.* 1986) of Infinity Two. The ASCOT5 code is a validated Monte-Carlo code that has been extensively used in interpretative and predictive modeling of fast-ion dynamics in tokamaks (Heikkinen *et al.* 1998, 2001; Kurki-Suonio *et al.* 2002; Hynönen *et al.* 2007; Kurki-Suonio *et al.* 2009; Snicker *et al.* 2012) and stellarators (Äkäslompolo *et al.* 2018). KORC-T is an open-source code that has been used to study the relativistic dynamics of runaway electrons in tokamaks (Carbajal *et al.* 2017; Carbajal & Del-Castillo-Negrete 2017; Del-Castillo-Negrete *et al.* 2018; Paz-Soldan *et al.* 2019), and more recently the fast-ion dynamics in the presence of magnetic islands in toroidal plasmas (Martinell & Carbajal 2022). We perform a benchmark between SIMPLE and ASCOT5 codes to compare estimates of collisionless alpha-particle losses and to identify the dominant loss mechanisms. Alpha-particles in ASCOT5 and KORC-T simulations are initialized in 3D space according to DT fusion-reactivity profiles consistent with plasma profiles (Bosch & Hale 1992). We use the AFSI code built into the Monte-Carlo ASCOT5 code to generate the initial spatial and velocity distribution of fusion-born alpha-particles. An extension to include finite Larmor effects in our analysis is done by simulating FO fusion-born alpha-particles with ASCOT5 and KORC-T. Unlike ASCOT5, KORC-T does not possess a capability to include a model for the wall; thus we only compare estimates of particle and energy losses at the plasma boundary as defined by the last closed flux surface (LCFS) of the free-boundary VMEC equilibrium. In both ASCOT5 and KORC-T simulations, we

use 3D magnetic fields that include the vacuum magnetic fields and the finite- β plasma contribution to the magnetic fields, encompassing the core plasma and the region between the LCFS and the wall. These are computed by the BMW code (Cianciosa 2024).

In the analysis of power loads to the walls of Infinity Two we use four models for the wall to assess the effect of wall shaping and its separation from the plasma on power loads due to alpha-particles. The first of these models is the standard Infinity Two wall (ITW), which is generated by computing a conformal envelope of the plasma that includes the magnetic islands of the island-divertor design of Infinity Two at the edge. The other three models use a three-dimensional extensions of the last closed flux surface (LCFS) as defined by a free-boundary VMEC equilibrium, each with different separation from the LCFS. To study the effect of collisionality at the scrape-off-layer (SOL) on power loads to the wall, we modify the plasma density and temperature profiles (Killer *et al.* 2019) at the SOL of Infinity Two plasmas. More complex effects at the SOL, such as the poloidal variation due to the island structure, the inclusion of neutrals or $E \times B$ drifts (Kriete *et al.* 2023) are not included in this work.

Finally, we assess the stability of alpha-particle driven AE activity in Infinity Two using the STELLGAP and FAR3d codes. For this, we use STELLGAP to compute the Alfvén continuum given by the profiles of the thermal plasma of Infinity Two. This analysis allows us to find the location in radius and frequency of Alfvén gaps in the plasma. Next, the stability analysis of AE occurring in these Alfvén gaps is performed using the FAR3d code. The slowing-down alpha-particle distribution obtained from ASCOT5 simulations is used for this calculation.

This paper is organized as follows: in Sec. 2, we describe the basic properties of Infinity Two stellarator design. In section 3, estimates of the core particle and energy confinement of alpha particles present in the Infinity FPP are provided based on orbit calculations. From these calculations, estimates for power loads on the walls are provided in Section 4. In section 5, the stability properties of Infinity Two with respect to Alfvén eigenmodes are addressed. Finally, a discussion of the major results from this work is provided.

2. Properties of Infinity Two stellarator design

In this work we evaluate alpha-particle transport and confinement in the Infinity Two FPP baseline plasma physics design (Hegna *et al.* 2025). Infinity Two is a quasi-isodynamic (QI) (Helander 2014) 4-field-period stellarator designed for reactor conditions. Plasma parameters used for this evaluation (Guttenfelder *et al.* 2025) include the peak electron density and temperature at the magnetic axis $n_{e,0} = 2.5 \times 10^{20} \text{ m}^{-3}$ and $T_{e,0} = 17.5 \text{ keV}$, a 50-50 D-T mix, and an assumed 5% He ash. This corresponds to a volume-average thermal plasma $\langle \beta \rangle = 1.6\%$ and alpha-particle beta $\langle \beta_\alpha \rangle = 0.31\%$, with an alpha-particle power of $P_\alpha = 158 \text{ MW}$ corresponding to a fusion power of $P_{fus} \approx 790 \text{ MW}$. The major and minor radii of this configuration are $R_0 = 12.5 \text{ m}$ and $a = 1.25 \text{ m}$. However, for this study we describe a confinement zone (with topologically toroidal flux surfaces) for a somewhat smaller plasma (with $a_{eff} = 1.1 \text{ m}$) from a free boundary VMEC calculation and use BMW to describe the fields outside this region which includes the presence of $N/M = 4/5$ divertor magnetic island.

In Fig. 1 we show the plasma profiles as function of the normalized radius, ρ . Here, $\rho = r/a = \sqrt{\psi/\psi_{LCFS}}$, with ψ the toroidal magnetic flux, and ψ_{LCFS} the toroidal magnetic flux at the LCFS. This plasma has a relatively flat density profile at the core, and concentrated alpha-particle power at $\rho \leq 0.7$ from fusion reactions following thermal plasma profiles. P_α is computed using Bosch-Hale reactivity of D-T plasmas (Bosch & Hale 1992). Note that the plasma profiles beyond the LCFS at $\rho = 1$, that is, in the

scrape-off layer (SOL), are kept constant in this simplified model. In other words, density, temperature and other plasma parameters at the SOL use the constant value found at the LCFS. This means constant collisionality for alpha-particles from the LCFS (magenta) up to the location of the wall, shown in Fig. 2. During operation, the fast-ion particles will actually travel through a very cold and dense region in the magnetic islands before passing into the far scrape-off layer. In this work, we did not attempt to self-consistently simulate the helically non-uniform edge structure but instead we analyze the sensitivity of the results to the SOL conditions by varying the plasma conditions.

For analyzing the sensitivity of our results on wall loads to SOL conditions, we generate an additional model for the plasma that includes an exponential radial decay of the plasma profiles in the SOL, see Fig. 1. That is, density and temperature profiles in the SOL have the following radial dependence

$$T(\rho) = T_{LCFS} \exp(-\rho/\lambda'), \quad (2.1)$$

$$n(\rho) = n_{LCFS} \exp(-\rho/\lambda'), \quad (2.2)$$

where $\lambda' = \lambda/a$ is the normalized radial decay length of the SOL, and λ is chosen to be of the order of $\lambda \sim 10$ cm. This value allows us to assess both alpha-particle transport and wall loads in a different collisionality regime (with respect to flat profiles at the SOL) and to obtain sensible values of plasma density $n \sim 10^{18} \text{ m}^{-3}$ and temperature $T \sim 1$ eV at the location of the farthest wall (outermost dashed line in Fig. 2). Notice that this radial decay of the plasma profiles is uniform along the helical direction, in contrast to the actual configuration which has a high degree of helical dependence due to the magnetic island.

We use the above models for the plasma to assess core confinement of alpha-particles and to obtain estimates of wall loads from alpha-particles leaving the core and ultimately hitting any of the walls shown in Fig. 2. Note that in these walls, the divertor components were not included. In Fig. 2 we also show Poincaré sections of the vacuum (left) and finite- β (right) magnetic fields for this configuration at half-field period, that is, at $\phi = 45^\circ$. The vacuum magnetic field is computed using currents in the coils of Infinity Two. The finite- β fields include the response from the plasma in addition to the vacuum magnetic fields. This is computed via the Biot-Savart Magnetic VMEC Vector-potential (BMW) code (Cianciosa 2024; Frerichs 2024). The BMW code uses Biot-Savart integration of the equilibrium current density to obtain a continuous magnetic vector potential everywhere. By combining the vacuum and plasma portions of the vector potential, the resulting total magnetic field can be evaluated from $\nabla \times \mathbf{A} = \mathbf{B}$ at any point in space (even beyond the VMEC boundary) and ensures divergence-free fields.

SIMPLE simulations are collisionless, guiding-center calculations used to provide a first estimate of alpha-particle losses in optimized configurations. Once a particular configuration is found to have promising alpha-particle confinement, a more detailed and computational expensive analysis follows using other set of codes such as ASCOT5 and KORC-T. The magnetic field for SIMPLE simulations is provided by a VMEC equilibrium. Particles are sourced on a single flux surfaces by selecting random locations along a field line. Each particle is given an isotropic starting velocity. Particles are followed until they either leave the LCFS indicating a lost particle or until a set amount of time has elapsed. We follow these alpha-particles in time for 0.1 seconds, which is enough time for analyzing prompt losses. SIMPLE simulations showed very low alpha-particle losses. Only 0.4% of the launched particles reached the LCFS.

SIMPLE is extremely quick to run and therefore can provide results for a vast number

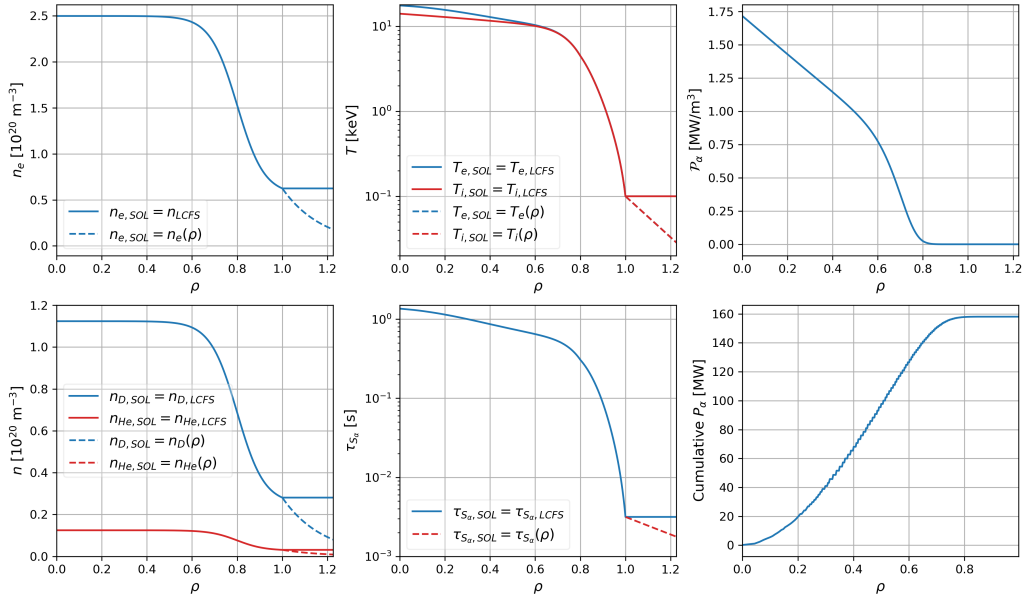


Figure 1: Plasma profiles of Infinity Two. Electron and ion density and temperature profiles using constant values at the SOL, $n_{SOL} = n_{LCFS}$ and $T_{SOL} = T_{LCFS}$, are shown with solid lines. Profiles using an exponential radial decay at the SOL, $n_{SOL} = n(\rho)$ and $T_{SOL} = T(\rho)$, are shown with dashed lines. We only show deuterium density profiles since tritium profiles are the same in this 50-50 D-T plasma. Radial profiles of alpha-particle power density, \mathcal{P}_α , and cumulative alpha-particle power, P_α , are the same for both flat and radially decaying profiles at the SOL. The slowing-down time of alpha-particles, $\tau_{S\alpha}$, spans several time scales from milliseconds to seconds.

of equilibria. However, while useful to verify a baseline of good confinement, these simulations are insufficient to characterize how a configuration will perform in realistic conditions. A more detailed analysis including a proper 3D birth distribution of alphas, the effect of collisions, and full-orbit effects is conducted to obtain more robust estimates of particle and energy losses of fusion-born alpha-particles as well as estimates of wall loads. This is presented in the following sections.

3. Core particle and energy confinement

In this section, we present an assessment of particle and energy confinement of fusion-born alpha-particles in Infinity Two core plasmas.

In Fig. 3 we show the initial location in the $\theta\phi$ -plane in VMEC coordinates of lost alpha-particles in a SIMPLE simulation of Infinity Two. These alpha-particles are initialized at $\rho = 0.55$. As can be seen from this figure, all lost particles are located in a region of relatively low magnetic field, $|B|$, indicating the poor orbits are due to deeply trapped particles. One of the design principles of Infinity Two is the alignment of B_{min} (and B_{max}) along the field as this provides robust collisionless guiding center orbit confinement. As shown in the right panel of Fig. 3, which shows a plot of $|B|$ along the field, that this design goal is largely produced. However, not all of the local B_{min} locations are perfectly aligned. In these regions, particles can be locally trapped with a non-zero bounce averaged radial drift.

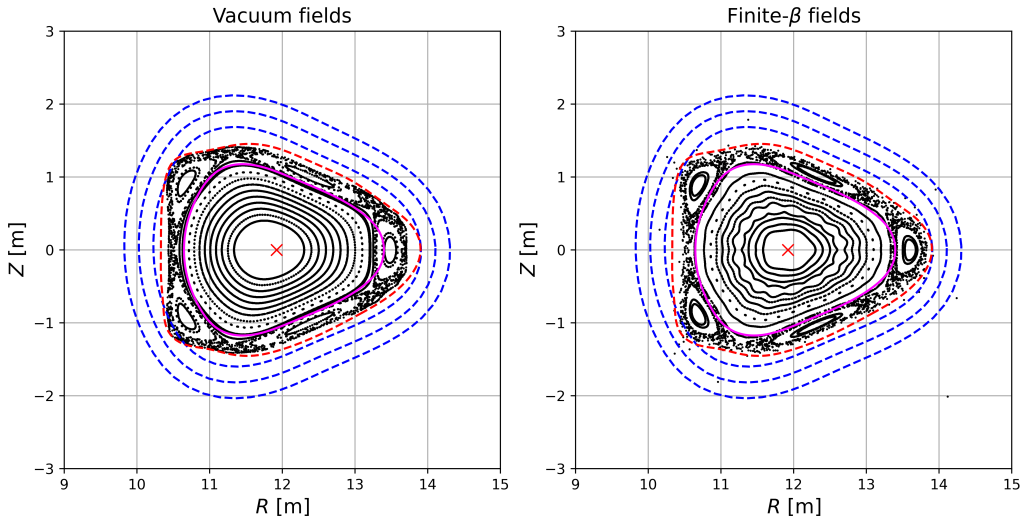


Figure 2: Poincaré sections of vacuum (left) and finite- β (right) magnetic fields of Infinity Two at half-field period, $\phi = 45^\circ$. The magenta line and red cross represent the LCFS and magnetic axis location, respectively, as obtained from the free-boundary VMEC equilibrium. The red dashed line show the location of the standard Infinity Two wall. The blue dashed lines show the location of the walls obtained from a three-dimensional extensions of the LCFS. We observe a small Shafranov shift in the finite- β magnetic field, seen on this poloidal section as a displacement of flux surfaces (black markers) towards the outboard side of Infinity Two. This is visible from comparing the location of flux surfaces in both cases with respect to the LCFS and the magnetic axis.

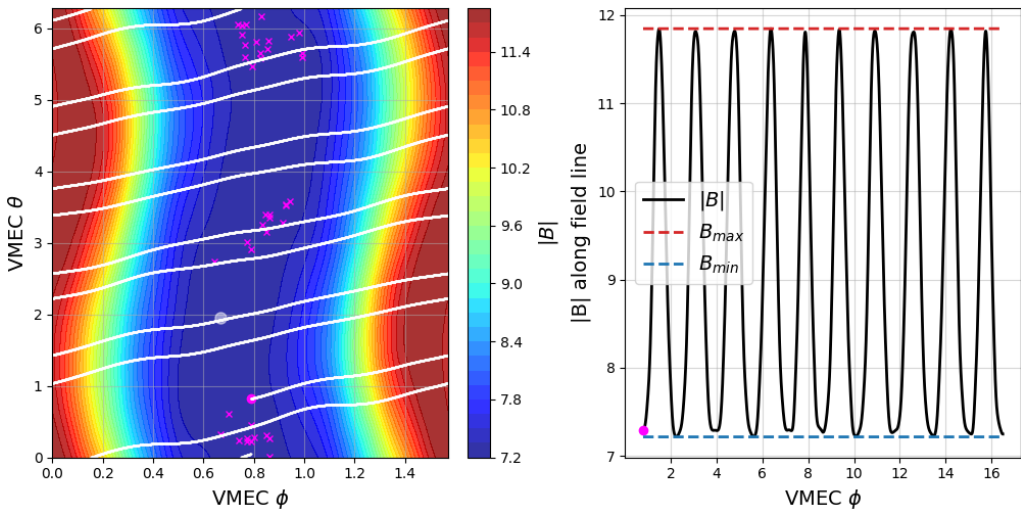


Figure 3: Isosurfaces of the magnitude of the magnetic field $|B|$ at the flux surface $\rho = 0.55$ (left), and an example of a magnetic field line starting in the well region (white trace on left panel). Initial location of simulated lost particles in Infinity Two are shown with magenta crosses. On the right panel we show the same magnetic field line in the left panel as a function of the toroidal angle (VMEC ϕ coordinate). In red and blue dashed lines are shown the global maximum and minimum values of $|B|$ at $\rho = 0.55$.

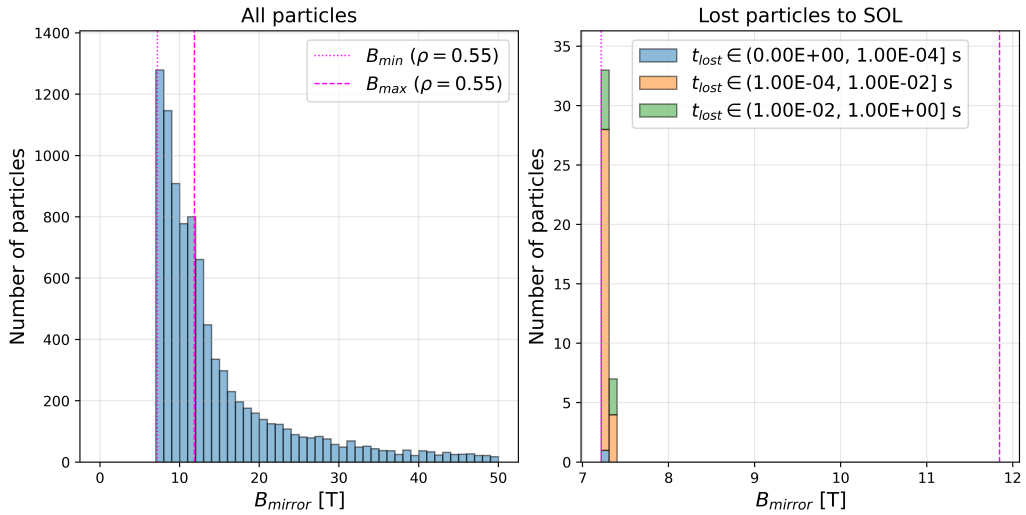


Figure 4: Orbit classification of simulated collisionless GC alpha-particles using the SIMPLE code.

To further illustrate the role of bad deeply trapped particle orbits on the confinement, we use results from collisionless guiding-center theory to classify particle orbits in SIMPLE simulations based on the magnitude of the magnetic field at which they are expected to be reflected (bounce), $B_{mirror} = \mathcal{E}_0/\mu$, where \mathcal{E}_0 is the initial (birth) energy of alpha-particles at 3.5 MeV, and μ the magnetic moment. Because orbits are collisionless, both quantities are assumed to be constant. In Fig. 4 we show the classification of an ensemble of 5000 simulated alpha-particles according to their value of B_{mirror} . Particles with B_{mirror} between the global minimum of $|B|$ at that flux surface, B_{min} , and the global maximum of $|B|$ at the same flux surface, B_{max} , are considered to be trapped alpha-particles. Those with $B_{mirror} > B_{max}$ are passing alpha-particles. After verifying that no passing particles are ever lost in the SIMPLE calculations, we only follow trapped particles. From these SIMPLE simulations, we observe that it is deeply trapped particles ($B_{mirror} \approx B_{min}$) that drive collisionless alpha-particle losses, see right panel of Fig. 4. In these simulations, we consider that an alpha-particle is lost to the SOL when it crosses the LCFS as defined by the free boundary VMEC equilibrium. Most of the losses occur prior to 10 milliseconds. Particles lost in this time region are expected to exit with most of their energy

The next step in our analysis of alpha-particle confinement in the core plasma is the use of the ASCOT5 code (Särkimäki 2019), which can be used to follow the collisionless and collisional dynamics of alpha-particles. For these simulations, the BMW code is used to convert the magnetic field components from the VMEC equilibrium onto the rectangular cylindrical grid that ASCOT5 uses. BMW includes both the vacuum magnetic fields from the coils of Infinity Two and the plasma contribution to the magnetic field. We have performed a benchmark test between SIMPLE and collisionless GC ASCOT5 simulations to verify that the different representations of the magnetic field do not result in different core alpha-particle confinement properties. In this test, we use the same initial isotropic distribution in pitch-angle of 3.5 MeV alpha-particles in both codes. Also, simulated alpha-particles are initialized at the same flux surface $\rho = 0.55$. We find good agreement between estimates of alpha-particle losses from SIMPLE and ASCOT5 simulations, being 0.4% for the former and 0.6% for the latter. As in SIMPLE simulations, ASCOT5

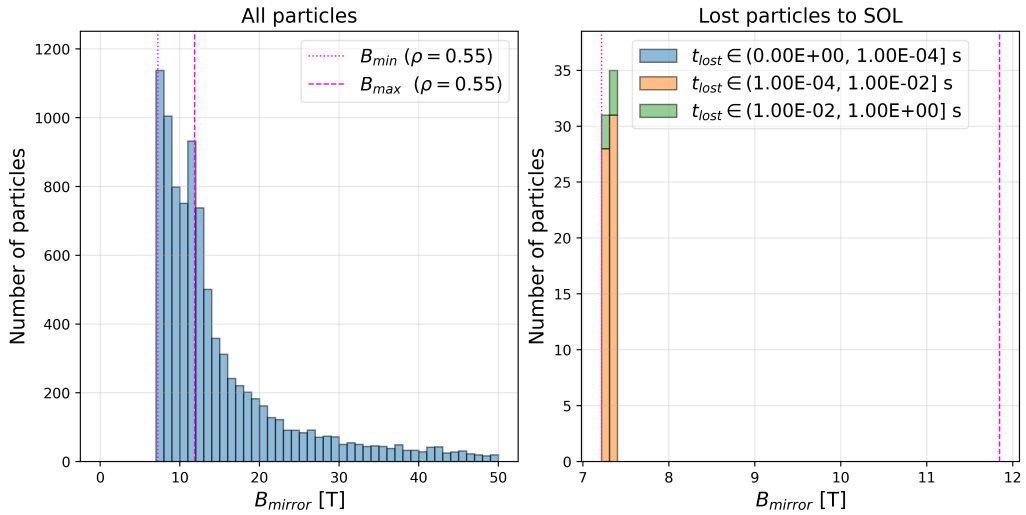


Figure 5: Orbit classification of simulated collisionless GC alpha-particles using the ASCOT5 code.

simulations predict that particle losses are driven by deeply trapped alpha-particles in Infinity Two, and are lost on the same time scales of hundreds of microseconds to tens of milliseconds, as shown in Fig. 5. This benchmark test provides confidence that the different representations of the magnetic field do not influence results of core alpha-particle confinement significantly.

We now simulate the dynamics of collisional alpha-particles in Infinity Two using ASCOT5. These simulated alpha-particles are initialized with an isotropic distribution for their initial pitch-angle and initial birth energy of $\mathcal{E}_0 = 3.5$ MeV, and are evolved in time until either they become locally thermalized with the background plasma via Coulomb collisions or are lost to the SOL, that is, when they cross the LCFS. Their initial spatial distribution follows the D-T fusion-reactivity distribution computed using the built-in AFSI code in ASCOT5, which applies the Bosch-Hale model (Bosch & Hale 1992) of D-T fusion reactions to thermal plasma profiles of Infinity Two. We observe that most alpha-particles are born in the core plasma at $\rho \leq 0.7$, with very few being born at the plasma edge. In addition, importance sampling is used to efficiently sample the initial distribution function of fusion-born alpha-particles. For this, each numerical particle is weighted according to the initial local alpha-particle density. In Fig. 6 we show an example of the initial spatial distribution of simulated alpha-particles in ASCOT5, generated as described above.

We also perform some FO simulations to study finite Larmor effects on alpha-particle confinement in Infinity Two. For this, we use the ASCOT5 and KORC-T codes. Both codes use the same initial conditions for the simulated alpha-particles, representation of the magnetic field, plasma profiles, and model for collisions between alpha-particles and the background plasma, which includes electrons, D, T, and He. Also, they use the same type of spline interpolations for the magnetic field components. They mainly differ in the algorithm for advancing in time the particles subject to the relativistic Lorentz force. ASCOT5 uses a volume-preserving algorithm (VPA) (Zhang *et al.* 2015) while KORC-T use a modified Boris algorithm (Vay 2008). Performing FO simulations with these two codes allow us to assess the effect of using different algorithms for solving the FO orbits on estimates of alpha-particle confinement.

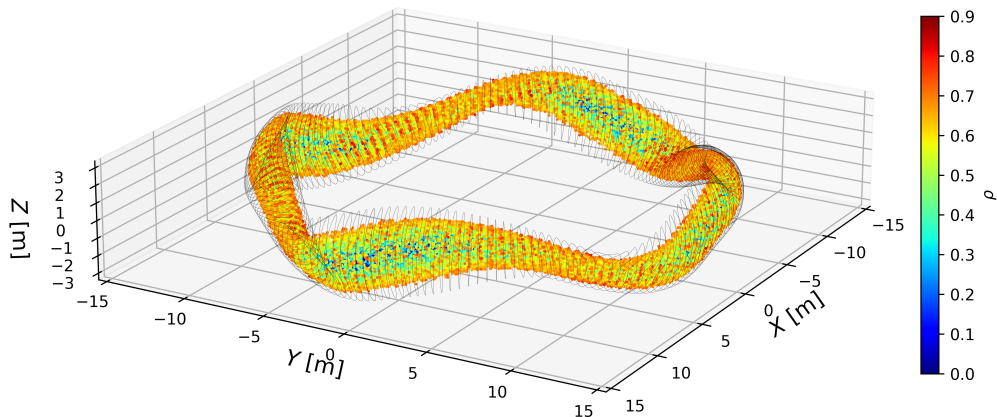


Figure 6: Initial spatial distribution of simulated alpha-particles in ASCOT5. Simulated alpha-particles are colored by their initial radial location (ρ) as show in the color bar on the right. The black lines show the location of the LCFS of the Infinity Two plasma at various toroidal angles.

In Table 1 we show estimates of core particle and energy losses from GC and FO ASCOT5 simulations as well as FO KORC-T simulations. As expected for the Monte Carlo approach to estimate particle confinement, we note that as we increase the number of markers we improve statistics of these estimates. Simulations using 10k markers already provide accurate particle and energy loss estimates in these simulations. From these collisional simulations we conclude that core alpha-particle energy losses are about 2% of the initial energy according to GC and FO ASCOT5 and around 4% according to FO KORC-T simulations. Particle losses are higher, around 8% of alpha-particles traced from the initial distribution according to GC and FO ASCOT5 simulations and 12% according to KORC-T simulation. Due to collisions with the background plasma, the simulated alpha-particles transfer some of their initial energy to the background plasma before they are lost to the SOL. We stress that the main difference between ASCOT5 and KORC-T simulations is the algorithm used to evolve the orbits of the particles. The discrepancy between ASCOT and KORC-T FO results highlight the difficulty involved in obtaining accurate and robust results for full-orbit calculations.

In Fig. 7 we show an attempt to classify lost GC and FO alpha-particles from simulations in Table 1 based on their initial value of B_{mirror} . Because collisions do not conserve energy and magnetic moment of particles, those that start on confined orbits, such as passing particles can be lost. However, these are lost after many collisions and thus long time scales. Most lost particles prior to 10 ms arise from the deeply trapped orbits, as was seen before in the collisionless GC case above, Fig. 5. There is a particular increase of lost particles near the trapped-passing boundary ($B_{mirror} \approx B_{max}$) with respect to collisionless SIMPLE and ASCOT5 simulations relative to what was seen in Figs. 4 and 5. Also, a small population of initially passing particles ($B_{mirror} > B_{max}$) are observed to be lost in these simulations, this likely due to collisions modifying their pitch angle, eventually turning them into trapped particles that leave the plasma.

In Fig. 8 we show the end states of energy of simulated collisional GC alpha-particles in ASCOT5. We stress that in these simulations of core alpha-particle confinement we

Particle losses [% of initial value]			
	1k markers	10k markers	100k markers
GC ASCOT5	5.18	7.82	7.75
FO ASCOT5	6.51	7.00	6.83
FO KORC-T	11.62	12.00	-

Energy losses [% of initial value]			
	1k markers	10k markers	100k markers
GC ASCOT5	1.35	2.26	2.31
FO ASCOT5	1.52	1.89	1.89
FO KORC-T	3.97	3.98	-

Table 1: Simulated particle and energy losses in core Infinity Two plasma.

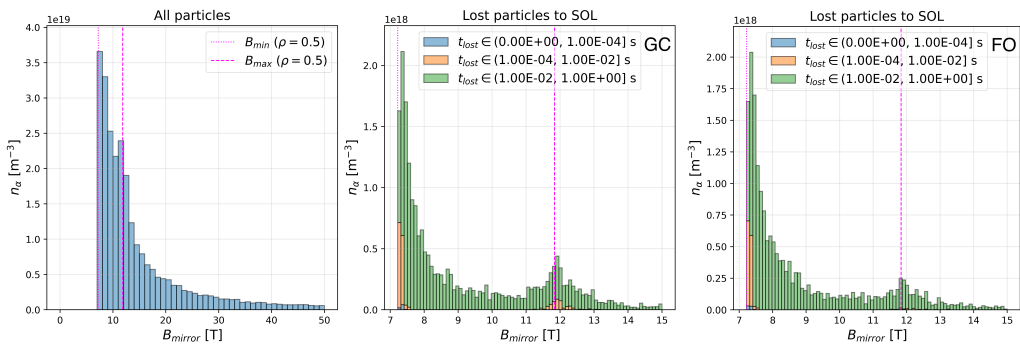


Figure 7: Orbit classification of simulated alpha-particles in ASCOT5: initial condition of all particles (left), initial condition of lost particles in collisional GC simulation (middle), and initial condition of lost particles in FO simulation (right).

follow the simulated particles in time until they either become thermalized with the background plasma (THERMAL) or until they get lost to the SOL by crossing the LCFS (RHOMAX). In the same figure we show the corresponding end states of simulated time of these alpha-particles. As it can be seen from this figure, most alpha-particle losses occur in time scales shorter than hundreds of milliseconds, $t_{sim} \leq 100$ ms, and mostly correspond to alpha-particles with relatively high energy, $\mathcal{E} \geq 100$ keV. FO ASCOT5 simulations show very similar results.

When we analyze the initial parameters of the distribution of lost alpha-particles in these simulations we find that their mean initial radial position is around $\rho = 0.54$ with very small mean pitch angle ($v_{\parallel}/v \approx 0$), initially located in the region of low magnetic field of Infinity Two ($\phi \approx 45^\circ$), corresponding to deeply trapped particles, see Fig. 9.

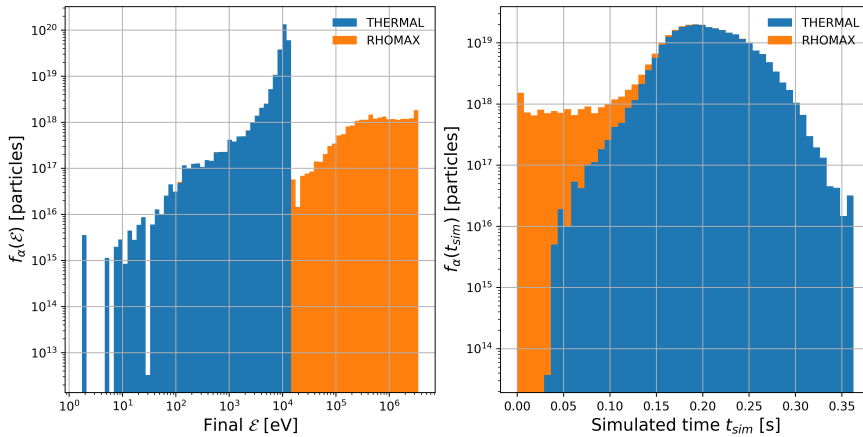


Figure 8: Energy (left) and simulated time (right) end states of GC alpha-particles in ASCOT5 simulation of core Infinity Two plasma. The sharp increase of $f_{\alpha}(\mathcal{E})$ at energies $\mathcal{E} \sim 10^4$ eV is expected, since confined alpha-particles thermalize via Coulomb collisions with the background plasma, where temperature is in the range of $T \sim 10^4$ eV.

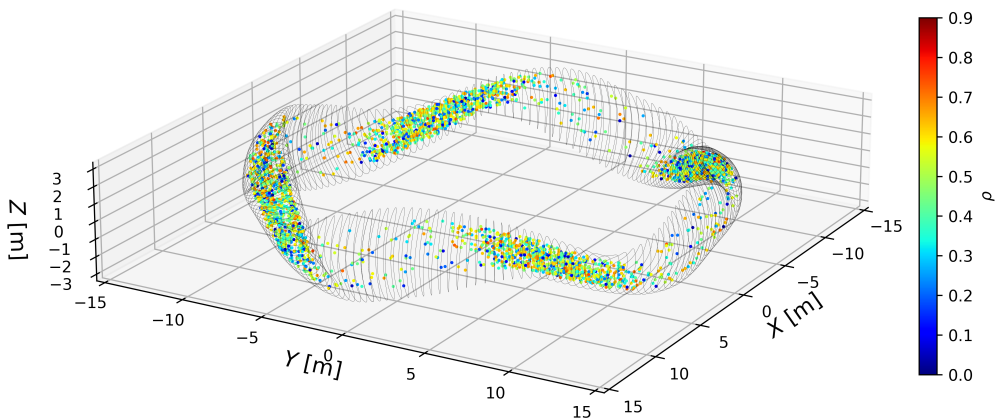


Figure 9: Initial spatial distribution of lost, trapped alpha-particles in ASCOT5. Consistent with the analysis of Fig. 3, most lost, trapped alpha-particles are located in the region of low magnetic field of Infinity Two, around $\phi = 45^\circ$. Simulated alpha-particles are colored by their initial radial location (ρ) as show in the color bar on the right. The black lines show the location of the LCFS of the Infinity Two plasma at various toroidal angles as a visual aid.

4. Power wall loads

Now, we analyze power loads on the Infinity Two wall due to alpha-particles losses. For this analysis, we use the same initial setup for ASCOT5 simulations described in the previous section. In this analysis, we only use GC simulations of alpha-particles. The number of particles required to obtain good statistics of power wall loads was too large to be simulated including FO effects. Furthermore, the loss characteristics between ASCOT GC and ASCOT FO were very similar, justifying the use of GC for this calculation. The ASCOT5 code has been extensively used in the past to study power wall loads due

to energetic ions on different tokamak devices, including reactor-relevant scenarios in ITER (Kurki-Suonio *et al.* 2002; Hynönen *et al.* 2007; Kurki-Suonio *et al.* 2009; Shinohara *et al.* 2011; Snicker *et al.* 2012; Kurki-Suonio *et al.* 2017).

For this analysis, we use four models for the wall that do not include any divertor structures. The first of these models corresponds to the standard Infinity Two wall (ITW). This wall is generated by computing a conformal envelope of the plasma that is outside the magnetic islands that are used for the island divertor. The average distance from this wall to the separatrix of the magnetic island chain is 10 cm and its total area is 1034 m². The other three models are obtained from a three-dimensional extensions of the last closed flux surface (LCFS) as defined by the free-boundary VMEC equilibrium described previously, using the methodology suggested in the appendix of (Landreman 2017). These three walls have different separation between the wall and the LCFS which we will refer to as the “wall gap”, Δ_w . We consider three values of Δ_w in our analysis: 30 cm, 50 cm, and 70 cm, corresponding to a total wall area of 1046 m², 1153 m², and 1263 m², respectively. These walls are transformed into a triangulation (tri-mesh) which is then passed to ASCOT5 for the simulations, each triangulation consisting of 50552 triangles. These models for the wall are intended to assess the sensitivity of the wall loads on the wall structure and to inform the later design of divertor structures and shielding of first wall components.

In Table 2 we show peak wall loads, particle and energy losses to the wall, and wetted area in Infinity Two plasmas for GC ASCOT5 simulations using different number of markers. Here, wetted area is defined as the sum of the areas of triangles of the discrete wall that have been hit by at least one alpha-particle. Particle and energy losses refer to alpha-particles being lost to the wall, unlike core losses in Sec. 3 which were defined as those alpha-particles crossing the LCFS ($\rho = 1.0$). The implications on the values of particle and energy losses from using this different definition is discussed below. From this table, we note that estimates of particle and energy losses are well described by simulations with as few as 1k markers. However, peak wall loads are not correctly described by simulations with fewer markers than 100k. Therefore, all results in the rest of this section refer to GC ASCOT5 simulations using 100k markers. Regarding the wetted wall area, this is a standard quantity used in past reactor-relevant analysis (Kurki-Suonio *et al.* 2017; Scott *et al.* 2020). However, we observe that this quantity depends on both the number of markers and area of triangles (via the number of triangles) used in the simulations. We do not observe convergence towards a value as for particle and energy losses, and peak wall loads. Rather, the wetted wall area keeps increasing as we increase the number of markers, although these new wetted areas with more markers correspond to wall loads of the order of kW/m² or lower. Thus, we report the wall wetted area in our simulations of Infinity Two only for completeness.

In Table 3 we show peak wall loads, particle and energy losses to the wall, and wetted area in Infinity Two plasmas using both flat plasma profiles at the SOL, see Fig. 1, and plasma profiles with exponential radial decay at the SOL, see Fig. 1. First, we note that both particle and energy losses are lower than the core alpha-particle losses discussed in Sec. 3. This is because once alpha-particles leave the core plasma and enter the SOL plasma they experience a more collisional plasma. These collisions stop (thermalize) some of these energetic alpha-particles in our ASCOT5 simulations before they hit the wall. This can be seen in Fig. 10 where we show the end state of energy and simulated time of alpha-particles for both the flat and plasma profiles with exponential radial decay at the SOL. While we observe that particle losses to the wall occur in similar time scale as core losses, see right panel of Fig. 8, the final distribution of simulated alpha-particles

Flat SOL plasma profiles

	Particle losses [%]	Energy losses [%]	Peak wall load [MW/m ²]	Wetted wall area [m ²]
1k markers	3.90	1.10	2.31	0.79
10k markers	3.40	1.10	5.15	4.92
50k markers	3.60	1.20	3.38	14.62
100k markers	3.70	1.20	2.17	20.44
500k markers	3.70	1.20	2.04	44.30

Table 2: Peak wall loads, particle and energy losses to the wall, and wetted area as function of number of markers in GC ASCOT5 simulations of wall loads in Infinity Two. All simulations reported in this table use a wall with $\Delta_w = 30$ cm, simulations using other wall model show the same trend.

Flat SOL plasma profiles

	Particle losses [%]	Energy losses [%]	Peak wall load [MW/m ²]	Wetted wall area [m ²]
ITW	5.00	1.50	2.51	18.83
$\Delta_w = 30$ cm	3.70	1.20	2.17	20.44
$\Delta_w = 50$ cm	3.10	1.10	2.28	18.58
$\Delta_w = 70$ cm	3.00	1.10	2.24	17.80

Exponential radial decay of SOL plasma profiles

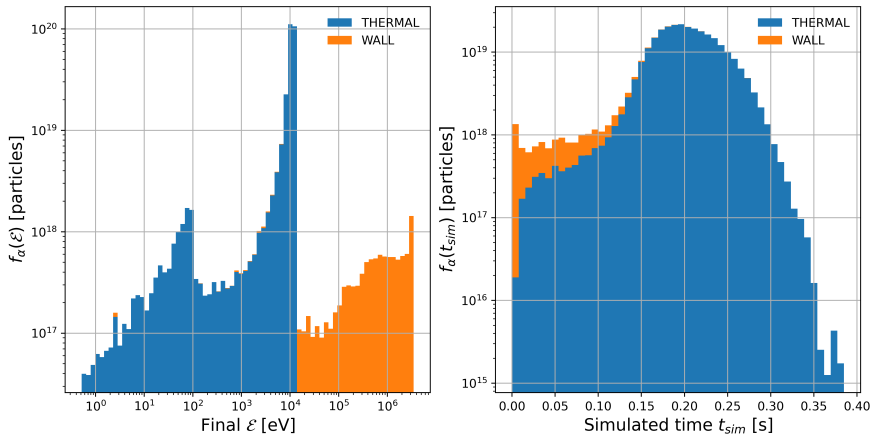
	Particle losses [%]	Energy losses [%]	Peak wall load [MW/m ²]	Wetted wall area [m ²]
$\Delta_w = 30$ cm	3.50	1.10	2.43	19.87
$\Delta_w = 50$ cm	3.00	1.10	2.45	16.69
$\Delta_w = 70$ cm	2.70	1.10	3.00	15.77

Table 3: Simulated peaked wall loads, particle and energy losses to the wall, and wetted area in Infinity Two plasmas. Results from GC ASCOT5 simulations using 100k markers.

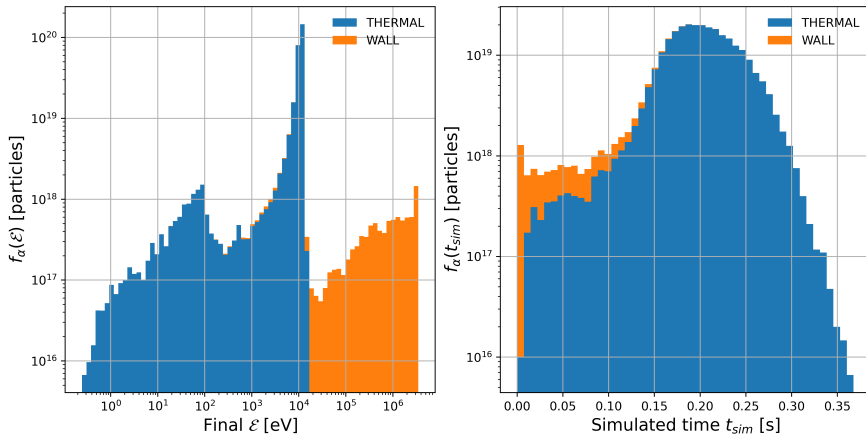
shows a larger population of particles in the range of energies from $\mathcal{E} = 1$ eV to $\mathcal{E} = 100$ eV due to alpha-particles interacting via Coulomb collisions with the SOL plasma.

Regarding estimates of peak wall loads, we observe lower values of this quantity for the wall with $\Delta_w = 30$ cm. Note that we only perform simulations of the ITW with flat SOL profiles. Given the proximity of the ITW to the LCFS, there is very little difference in the analysis when different SOL profiles are used. We note that for these cases with lower peak wall loads, we obtain the largest wetted areas. This suggests that wall loads are reduced when alpha-particle losses to the wall are spread over wider wall areas.

In Fig. 11 we show the power wall loads on the $\theta\phi$ -plane for simulations with $\Delta_w = 30$ cm, $\Delta_w = 70$ cm, and the ITW for flat SOL plasma profiles. In these figures, the positions of wall elements (triangles) are mapped onto the $\theta\phi$ -plane, and are colored according to the power load computed by ASCOT5. In all simulations, we observe higher power loads



(a) Flat plasma profiles at the SOL of Fig. 1



(b) Radially decaying plasma profiles at the SOL of Fig. 1

Figure 10: Energy (left) and simulated time (right) end states of GC alpha-particles in ASCOT5 simulation using flat (a) and radially decaying (b) plasma profiles at the SOL. The sharp increase of $f_\alpha(\mathcal{E})$ at energies $\mathcal{E} \sim 10^4$ eV is expected, since confined alpha-particles thermalize via Coulomb collisions with the background plasma, where temperature is in the range of $T \sim 10^4$ eV.

around $\phi = 60^\circ$, with different poloidal locations. From the analysis of Sec. 3, we observe that most lost alpha-particles are deeply trapped particles with $B = B_{mirror} \approx 7.5$ T, initially at radial location $\rho \approx 0.5$ and toroidally localized around $\phi = 45^\circ$, the region of low magnetic field of Infinity Two, see Fig. 9. We compute the location of the reflection points of these particles by calculating the angle ϕ at which $|\bar{B}|(\phi) = B_{mirror}$ at $\rho = 0.5$. We find that these occur at $\phi \approx 30^\circ$ and $\phi \approx 60^\circ$. This suggests that these particular alpha-particles radially drift outwards around those toroidal locations, crossing the LCFS and escaping the core plasma around the poloidal location of the x-points. Also, we observe the 4-field-period periodicity of the wall loads patterns, but stellarator symmetry (Dewar & Hudson 1998) is broken, as observed in previous works (Lazerson *et al.* 2021*b,c*). Our analysis shows that this asymmetry is caused by ∇B drifts, which for positive ions and the toroidal field pointing clockwise in Infinity Two effectively points downwards, according to our simulations. Thus, peak wall loads being localized around

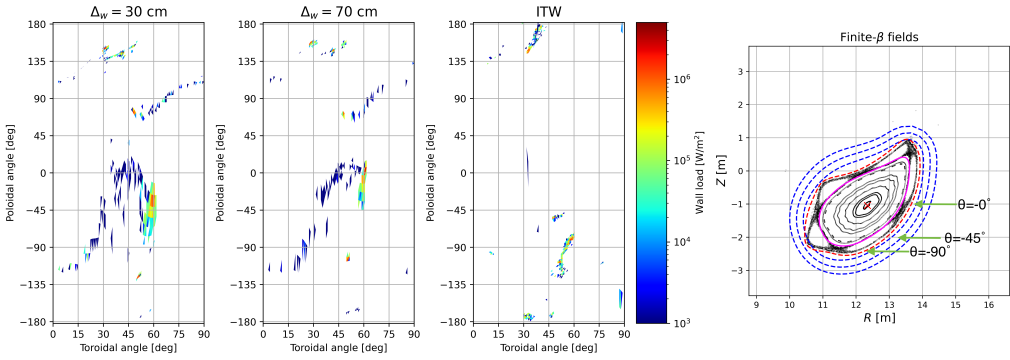


Figure 11: Power wall loads on the $\theta\phi$ -plane for flat SOL profiles for wall with $\Delta_w = 30$, $\Delta_w = 70$, and for the ITW. Only the first field period ($0^\circ \leq \phi \leq 90^\circ$) is shown given the 4-field-period periodicity of wall loads in ASCOT5 simulations. Poincaré sections of Infinity Two at $\phi = 60^\circ$ in the right panel show the approximate poloidal locations, θ , where peak wall loads occur.

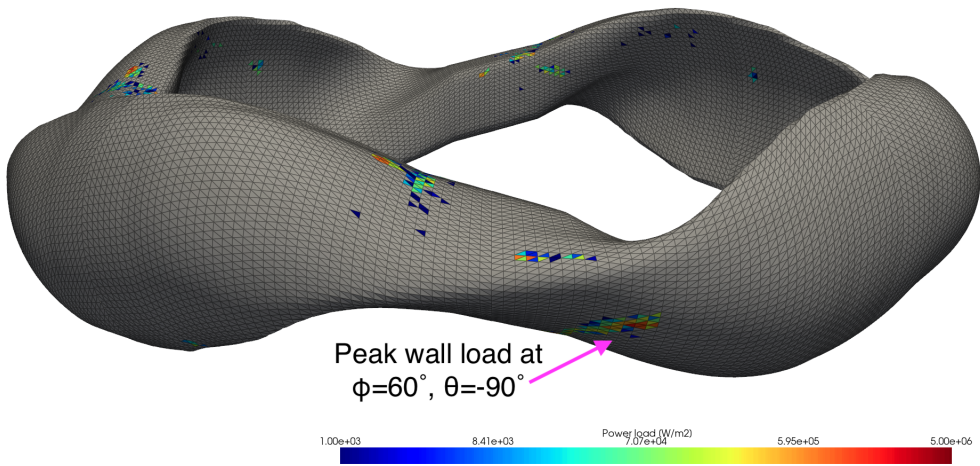


Figure 12: Power wall loads of ASCOT5 simulation using the ITW in 3D geometry. The edges of the triangles used in ASCOT5 simulations are shown in black. Reddish triangles show wall elements with higher values of power loads. Grey triangles show wall elements with negligible (below 1 kW/m^2) power loads.

$\phi = 60^\circ$ and $\theta < 0^\circ$. A test ASCOT5 simulation of Infinity Two using negative charged alpha-particles confirm this, showing the same 4-field-period periodicity, similar wall load values, but with peak wall loads now localized at $\phi = 30^\circ$ and $\theta > 0^\circ$, as expected from ∇B drifts. In Fig. 12 we show power wall loads in 3D for the ASCOT5 simulation using the ITW. Peak wall loads are shown with an arrow, other hot spots in the MW/m^2 range are visible in other locations but these are lower than the peak value of 2.51 MW/m^2 for this wall.

From this analysis we conclude that the lowest peak wall loads due to alpha-particles losses to the wall are found to be around 2.17 MW/m^2 , for the wall with $\Delta_w = 30$, with

localized poloidal position close to the x-point of the magnetic island chain outside the plasma volume of Infinity Two, see right-most panel of Fig. 11. Other power loads in these simulations are in the range of tens of kW/m² to hundreds of kW/m². It is expected that these peak power loads can be accommodated by existing helium-cooled plasma facing component technologies, either through the use of specialty FW tiles (Arbeiter *et al.* 2017) or helium cooled limiters (Noraajitra *et al.* 2015). Further, this suggest that there might be an optimal shaping and separation between the wall and plasma volume that can reduce peak power loads with respect to the standard ITW. Different collisional conditions at the SOL seem to modify peak wall loads by modifying slightly the wetted area but preserving the same patterns on the $\theta\phi$ -plane.

5. Stability of Alfvén eigenmodes

In this section, we assess the Alfvén eigenmode (AE) activity driven by alpha-particles in Infinity Two. Alfvén waves are ubiquitous collective modes supported by thermal plasma in the presence of a magnetic field. The frequency at which Alfvén waves occur depends on local plasma conditions. In the case of toroidal plasmas with radial plasma profiles and sheared magnetic fields, the wave frequency follows a radial dependence, too. This is known as the Alfvén continuum. In these plasmas, coupling between counter-propagating Alfvén waves might occur due to the toroidal and/or poloidal periodicity of the magnetic field, leading to regions in frequency where these Alfvén waves can not exist. This as the result of destructive interference between coupled waves. These regions are known as Alfvén gaps (Heidbrink 2008). In these gaps, radially extended, weakly damped modes might be driven unstable by alpha-particles. We aim to identify these modes in Infinity Two, if any, that may affect the confinement of fusion-born alpha-particles and cause inefficient plasma heating and enhancement of wall loads.

For this, we use the STELLGAP code to compute the Alfvén continuum and Alfvén gaps of Infinity Two. The FAR3d code is used to assess the stability of the dominant and sub-dominant Alfvén eigenmodes existing in these gaps. The FAR3d code solves a reduced set of equations for high-aspect ratio plasmas and moderate β -values (of the order of the inverse aspect ratio), retaining the toroidal angle dependency in an exact three-dimensional VMEC equilibrium. In these simulations, we include the effects of finite Larmor radius (FLR) damping effects of thermal and energetic ions as well as electron-ion Landau damping. The free-energy source of alpha-particle destabilization of AE is provided to FAR3d via moments of the gyro-kinetic distribution function of the alpha-particles, specifically, the alpha-particle density and their average parallel velocity. The correct model calibration requires performing gyro-kinetic simulations to calculate the Landau closure coefficients in the gyro-fluid simulations, matching the analytic TAE growth rates of the two-pole approximation of the plasma dispersion function with a Lorentzian energy distribution function for the energetic particles. This calibration has been done for DIII-D tokamak geometry by matching the gyro-fluid response function with its kinetic analog for a parallel propagating Alfvén wave (Spong 2013). The lowest order Lorentzian can be matched either to a Maxwellian or to a slowing-down distribution by choosing an equivalent average energy. In our assessment, we use a Maxwellian distribution for the alpha-particles using a temperature that matches the moment-averaged temperature of the simulated alpha-particle distribution, see discussion in Sec. 2.3 of Varela *et al.* (2024d). Previous benchmarking studies validated FAR3d code results with the gyro-kinetic codes EUTERPE, GEM, GTC, GYRO and ORB, with the hybrid code MEGA, and with the perturbative eigenvalue NOVA-K, see Ref. (Taimourzadeh *et al.* 2019) for details. The FAR3d code has been validated against experimental

measurements in helical plasmas such as LHD (Varela *et al.* 2017b, 2019a, 2020a, 2021, 2022b, 2024b,a), TJ-II (Varela *et al.* 2017a; Cappa *et al.* 2021; Eliseev *et al.* 2021), and Heliotron J (Yamamoto *et al.* 2020; Varela *et al.* 2020b, 2022a). Similarly, validation against experimental measurements in tokamak plasmas such as DIII-D (Pace *et al.* 2018; Varela *et al.* 2018, 2019b; Huang *et al.* 2020; Spong *et al.* 2021; Ghai *et al.* 2021), EAST (Wang *et al.* 2023; Sun *et al.* 2024), and JET (Garcia *et al.* 2024), has also been done.

Figure 13(a), shows the rotational transform of Infinity Two, which is optimized to avoid major resonant surfaces in the core and to resonate with the $n/m = 4/5$ surface at the edge. Figure 13(b) show the radial profile of alpha-particle density and energy used for this assessment. These distributions are taken from a collisional GC ASCOT5 simulation at $t = 50$ ms. At this time in the simulation the alpha-particles have redistributed in the core plasma following drifts and start to slow-down, with peak energy of around 2.0 MeV at the magnetic axis and mean average energy of the entire distribution of 1.48 MeV. These alpha-particles have an average velocity of $v_\alpha/V_A \sim 0.7$ at the core and $v_\alpha/V_A \sim 0.3$ at the edge, suggesting that alpha-particles can potentially drive instabilities. Thus, the importance of performing this stability analysis. Here, V_A is the local Alfvén velocity. In panel (c) of this figure we analyze the contribution of alpha-particles of the slowing-down distribution (Alonso *et al.* 2022) with different energies (red filled circles) to the total $\langle\beta_\alpha\rangle = 0.31\%$ (black star). These $\langle\beta_\alpha\rangle$ for different energy ranges of the alpha-particle distribution are the ones used in the analysis of Sec. 5.1 where the stability limit of Infinity Two is explored. The geometry of Infinity Two is included in STELLGAP and FAR3d simulations via Boozer coordinates of the free-boundary VMEC equilibrium. The normalized radius is discretized using 200 radial points. Our sensitivity analysis varying the number of radial points show this is already enough resolution to compute the Alfvén continuum with STELLGAP and to perform the stability analysis of FAR3d.

In Fig. 14 we show the Alfvén gap structure of Infinity Two computed by STELLGAP for $n = 0, 1$ and 2 mode families. Here, a given mode family $n = k$ is defined as $n = k \bmod N$, where $N = 4$ is the magnetic field periods of Infinity Two. The Alfvén gaps are calculated for the modes $n = 0, 4, 8, 12, 16, 20, 24, 28$, $n = 1, 3, 5, 7, 9, 11, 13, 15, 17, 19, 21, 23, 25, 27$ and $n = 2, 6, 10, 14, 18, 22, 26$, including the coupling with the sound wave (BAE gap). In panel (a) of this figure we show the complete Alfvén gap structure including all three mode families. In panel (b) we show the Alfvén gap structure only for the $n = 0$ mode family. In panels (c) to (e) we separate the spectra to show the details of panel (b), and to label some of the Alfvén gaps as reference. In panels (f) to (i) we do the same for mode family $n = 1$, and in panels (j) to (m) for mode family $n = 2$. Wide BAE gaps cover all the minor radius ($\rho = 0.0 - 0.75$) in the frequency range of 5 – 50 kHz. There are TAE gaps from the inner to outer plasma region in the frequency range of 60 – 100 kHz. In addition, broad EAE gaps are observed above 100 kHz.

In Fig. 15 we show the expected helical gaps in Infinity Two as computed by STELLGAP. These gaps are located in the plasma periphery where no significant alpha-particle density gradient is observed from ASCOT5 simulations. Thus, destabilization of helical AEs by alpha-particles in these gaps is not likely to occur.

The stability assessment of AE that might occur in the Alfvén gaps obtained from STELLGAP simulations is now performed with FAR3d. The stability assessment includes the modes $n = 1, 3, 5, 7, 9, 11, 13$ and $n = 2, 6, 10, 14$.

The stability of AE modes in Infinity Two is mainly determined by the following factors: (1) the alpha-particle $\langle\beta_\alpha\rangle$, driving the strength of the perturbation, (2) Alfvén continuum damping, dictated by the magnetic field structure and thermal plasma profiles, (3) FLR

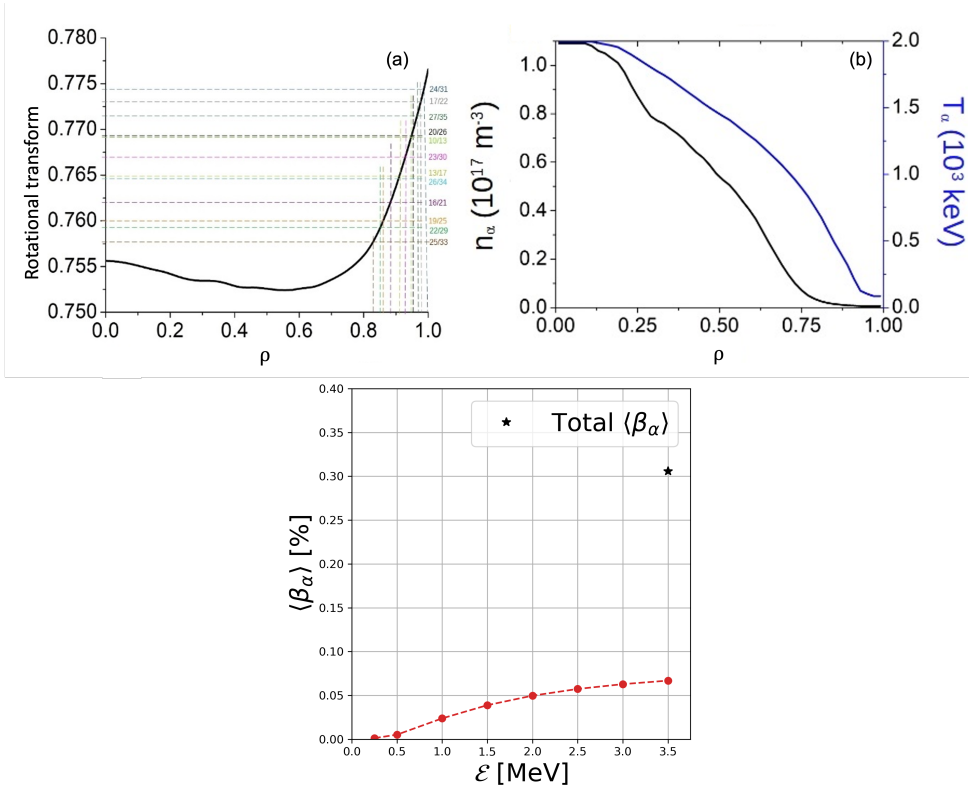


Figure 13: Panel (a): Iota profile of Infinity Two. The dashed colored vertical and horizontal lines indicate the radial location of the main rational surfaces. Panel (b): alpha-particles density (black line) and energy (blue) radial profiles in FAR3d simulations. Panel (c): total alpha-particle beta $\langle \beta_\alpha \rangle$ (black star), and $\langle \beta_\alpha \rangle$ for alpha-particles with different ranges of energies (red filled circles) according to a theoretical slowing-down distribution function (Alonso *et al.* 2022). Here, the total $\langle \beta_\alpha \rangle$ is the sum of the $\langle \beta_\alpha \rangle$ for alpha-particles with different energies. Note that $\langle \beta_\alpha \rangle$ is very small ($< 10^{-3}\%$) for alpha-particle energies $\mathcal{E} < 1.0$ MeV.

damping effects, and (4) electron-ion Landau damping. In Infinity Two, Alfvén continuum damping plays a relatively small role on reducing the radial extent of perturbations due to its weak magnetic shear (Varela *et al.* 2024c). Our FAR3d simulations with the alpha-particle density and energy profiles shown in Fig. 13 indicate the absence of unstable AE in the Alfvén gaps of Infinity Two, this as the result of its low alpha-particle beta $\langle \beta_\alpha \rangle = 0.31\%$, not being large enough to drive any AE unstable.

5.1. Stability limit of Infinity Two

Finally, we address the issue of finding the stability limit of Infinity Two to AE activity driven by fusion-born alpha-particles. This analysis provides information about trends of AE stability of Infinity Two away from its nominal steady-state operational regime. For this, we performed a parametric analysis varying beta of the simulated alpha-particle population. We perform this analysis for $\langle \beta_\alpha \rangle = 0.2\%$, 0.5% , 1.0% , and 2.0% . We note that when setting a value of $\langle \beta_\alpha \rangle$ we can either choose to keep fixed alpha-particle density and modify their energy, or to keep fixed energy and modify the alpha-particle density.

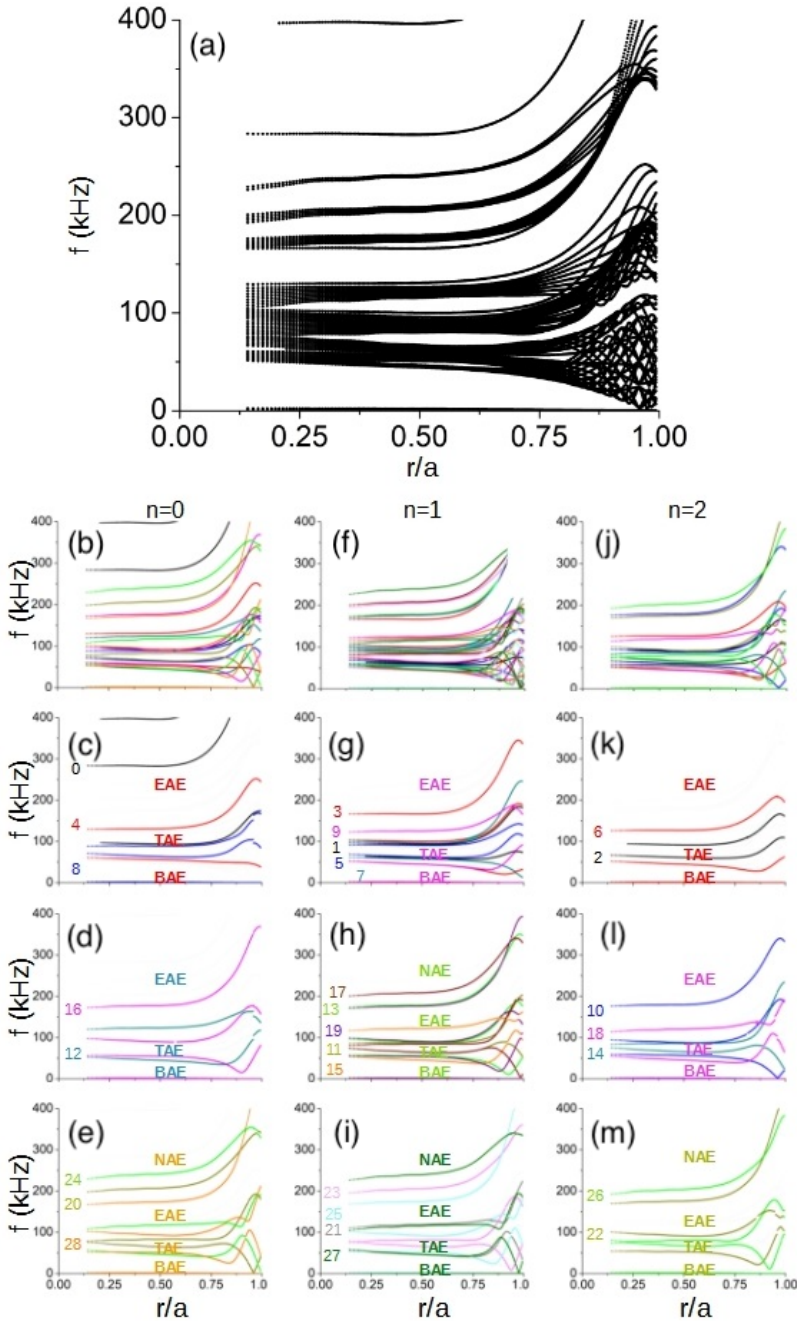


Figure 14: Alfvén gap structure of Infinity Two. Panel (a) shows the complete spectra of Alfvén modes. Panels (b), (f), and (j) show the same spectra but separating mode families $n = 0$, $n = 1$, $n = 2$, respectively. Panels (c) to (e) break down the spectra of panel (b) so we can label some of the computed Alfvén gaps as reference. In a similar way, panels (g) to (i) show the details of panel (f) for the mode family $n = 1$, and panels (k) to (m) show the details of panel (j) for the mode family $n = 2$.

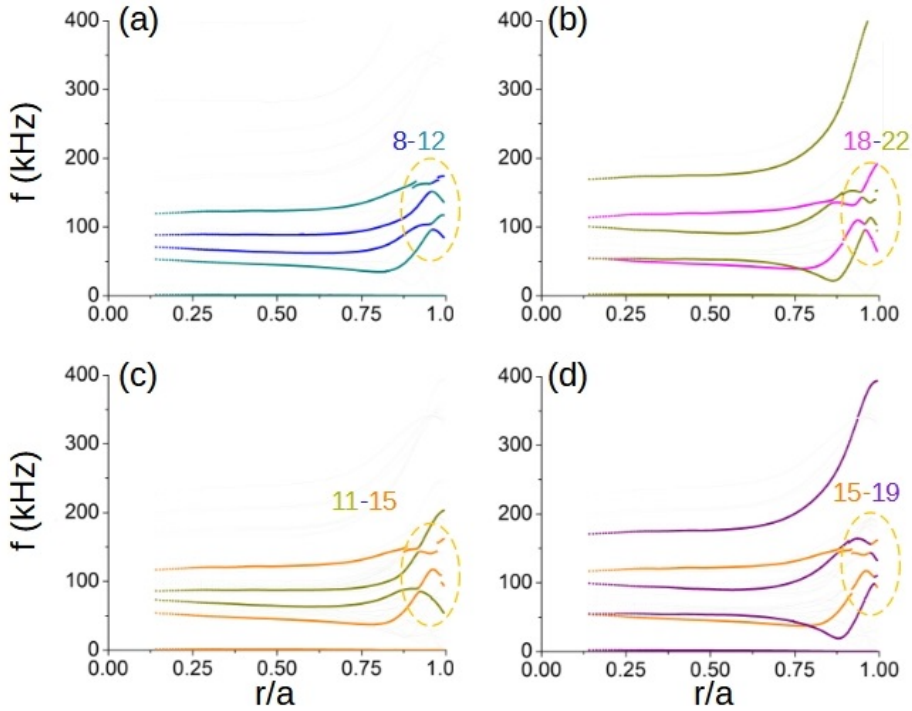


Figure 15: Helical Alfvén gaps in Infinity Two. Orange dashed oval indicates the radial location and frequency range of the helical gaps.

In this analysis we follow both approaches to mimic the effects of two populations of alpha-particles: relatively low-density and high-energy alpha-particles corresponding to alpha-particles in the early slowing-down phase, and higher density and relatively low-energy alpha-particles corresponding to alpha-particles in the late slowing-down phase. The shape of the alpha-particle profile of Fig. 13 is kept fixed in this analysis, given that the profile shape is not observed to change significantly for alpha-particles with energies ranging from 3.5 MeV down to 0.5 MeV in our ASCOT5 simulations. In a similar way to our analysis above, our FAR3d simulations for this parametric analysis use Maxwellian distributions with a temperature that matches the moment-averaged energy of the analyzed alpha-particle population. Specifically, we analyze AE driven by alpha-particles with $\mathcal{E} = 0.25, 0.50, 1.0, 1.5, 2.0, 2.5,$ and 3.0 MeV, that is, the same energies for which we calculate $\langle\beta_\alpha\rangle$ in Fig. 13(c). Also, we keep thermal plasma profiles and magnetic configuration fixed.

Our parametric analysis indicates that at high $\langle\beta_\alpha\rangle$ particles in the early-slowning-down phase ($\mathcal{E} = 1.5$ MeV to 2.0 MeV) lead to destabilization of dominant low-frequency AEs, between 30-40 kHz, falling into the frequency range of BAEs. The critical value of $\langle\beta_\alpha\rangle$ for the destabilization of these AEs is $\langle\beta_\alpha\rangle = 0.5\%$, increasing to $\langle\beta_\alpha\rangle = 1.0\%$ as we decrease the alpha-particle energy down to $\mathcal{E} = 1.5$ MeV. These critical values of $\langle\beta_\alpha\rangle$ fall well above the operational $\langle\beta_\alpha\rangle = 0.31\%$ of Infinity Two for beta values of alpha-particles with $\mathcal{E} \geq 1.5$ MeV.

On the other hand, alpha-particles in the late slowing-down phase ($\mathcal{E} < 1.5$ MeV) show the destabilization of AEs above 70 kHz, corresponding to the the frequency range of the TAE gap and lower bound of the EAE gap. Nevertheless, if the $\langle\beta_\alpha\rangle$ is large

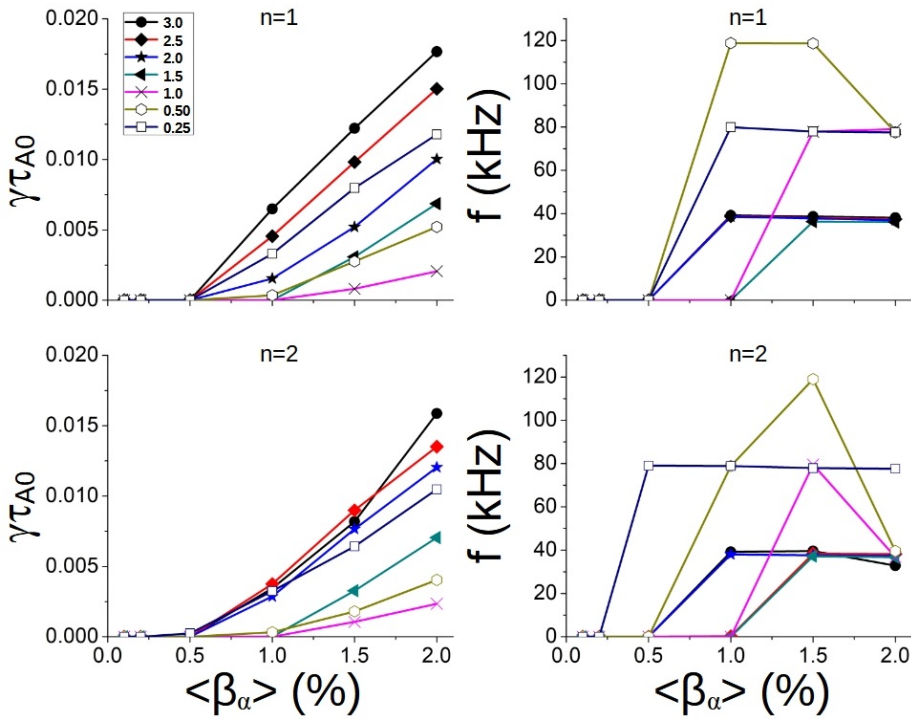


Figure 16: (a) Growth rate and (b) frequency of dominant AE destabilized by the $n = 1$ mode family. (c) Growth rate and (d) frequency of the dominant AE destabilized by the $n = 2$ mode family

enough, BAEs are the dominant instability. The critical value of $\langle\beta_\alpha\rangle$ for destabilization of these modes is $\langle\beta_\alpha\rangle = 1.0\%$ for the $n = 1$ mode family. The critical $\langle\beta_\alpha\rangle$ decreases to $\langle\beta_\alpha\rangle = 0.5\%$ for alpha-particles with $\mathcal{E} < 0.5$ MeV. The frequency of the dominant mode in this case is close to 120 kHz. We observe similar trends and mode structure for the unstable modes of the $n = 2$ mode family. Importantly, GAEs are also identified in the parametric analysis, although their growth rates are smaller compared to BAE and TAE. Thus, GAEs are not the most limiting stability for the device performance.

In Fig. 16 we show the growth rates and frequency ranges of dominant modes identified from this analysis driven by alpha-particles with different energies when their beta is varied. The observed trend for growth rates of these dominant modes is that these increase as we increase alpha-particle beta, this being the main mechanism for destabilization of AEs in Infinity Two. The analysis of dominant AEs also indicates that the resonance induced by alpha-particles in the early-slowng-down phase lead to the destabilization of BAEs, while alpha-particles in the late slowng-down phase can trigger higher frequency modes in the range of the TAE and EAEs. BAEs shows a larger growth rate compared to the TAE and EAE.

From this analysis we conclude that the required alpha-particle betas required to destabilize AEs in Infinity Two are much higher than those from its base operational regime, showing strong stability against AE activity. Importantly, we note that from past validation of FAR3d against gyro-kinetic simulations, these trends of stability are expected to hold.

6. Discussion

In this work we assessed alpha-particle transport and confinement in the 4-field-period optimized quasi-isodynamic (QI) stellarator Infinity Two. The generation of this optimized configuration relied on a program of aligning second adiabatic invariant contours with contours of the flux surface and the alignment of both B_{max} and B_{min} along the field line. Moreover, the Infinity Two configuration is also shown to have small values of the energetic particle confinement metric $\Gamma_c < 0.02$ for $\rho < 0.8$. All of these features portend excellent collisionless guiding center orbits for Infinity Two.

Collisionless SIMPLE and ASCOT5 simulations of GC alpha-particles showed particle losses less than 1% in the core Infinity Two plasma. Deeply trapped alpha-particles with small pitch-angle, $v_{\parallel}/v \approx 0$, dominate the losses in these simulations. Collisional simulations with alpha-particle distribution functions consistent with Infinity Two's reactivity profile using both GC and FO alpha-particles estimate less than 8% particle losses and less than 4% energy losses in the core plasma. Deeply trapped particles dominate particle and energy losses with other trapped particles, some close to the trapped-passing boundary, contributing to the losses. In this case, Coulomb collisions modifying the pitch-angle of alpha-particles work as a source of particles for the region of small pitch-angles that dominate losses. We observed that most alpha-particles are lost within few tens of milliseconds, still carrying relatively high energies, $\mathcal{E} \geq 100$ keV.

We evaluated power wall loads due to lost alpha-particles using GC ASCOT5 simulations. For this we used a simple wall model corresponding to a three-dimensional extension of the LCFS from the free-boundary VMEC equilibrium of Infinity Two. We found that when the distance between the wall and the core plasma is about $\Delta_w = 30$ cm we obtain the lower peak power loads, about 2.17 MW/m². These power loads are well within the technological capabilities of high-heat flux plasma facing components. When we varied the collisionality of the SOL plasma in Infinity Two by changing the plasma profiles in that region, we observed negligible variations in peak power loads. This showed that even when collisional effects at the SOL are important for stopping energetic alpha-particles from reaching the wall, their contribution to energy wall loads was insignificant. In all cases, peak wall loads are observed to occur around $\phi = 60^\circ$ with varying poloidal locations coinciding with the location of x-points of the magnetic island chain $n/m = 4/5$ at the edge of Infinity Two. These, are mainly produced by MeV alpha-particles corresponding to deeply trapped particles in the region of low-magnetic field. These particles, drift radially outwards around their reflection points at $\phi \approx 30^\circ$ and 60° , until they eventually cross the LCFS, escaping the core plasma in the vicinity of the x-points of the magnetic island chain, by a combined effect of drifts and collisions with the background plasma. Also, the wall loads from these simulations show the 4-field-period periodicity of Infinity Two but stellarator symmetry is broken, likely due to ∇B drifts. These results are intended to help design of first wall components and shielding of Infinity Two in the future. Also, we note that full-orbit effects were not included in the analysis of wall loads. Full-orbit effects need to be included in order to obtain more robust estimates.

The calculation of the Alfvén continuum of Infinity Two using the STELLGAP code showed the existence of TAE, BAE, EAE, and Helical Alfvén gaps at different frequency and radial locations. However, the stability assessment performed with FAR3d of Alfvén eigenmodes driven by alpha-particles in these gaps show the absence of unstable AE. This, due to the low alpha-particle beta $\langle \beta_\alpha \rangle = 0.31\%$ of the base 800 MW DT power scenario is not large enough to destabilize AE in the plasma. Our parametric analysis to identify the stability limit of Infinity Two shows that critical alpha-particle betas of

$\langle\beta_\alpha\rangle > 0.5\%$ are required to destabilize AEs in the BAE, TAE, and EAEs frequency range, much higher than the planned operational $\langle\beta_\alpha\rangle = 0.31\%$ of Infinity Two.

We have yet to perform a detailed coil sensitivity study to determine the sensitivity of the good energetic particle confinement to field perturbations. However, from an MHD equilibrium and stability standpoint, small field error effects should not produce dramatic changes as the rotational transform profile avoids major resonances and the operational β is far from stability limits.

Acknowledgments

This work was supported by Type One Energy. ASCOT5 development was partially funded by the Academy of Finland projects No. 353370, 324759, and 362342. The authors thank Mark R. Cianciosa at ORNL for useful discussions on usage of the BMW code. We thank Don Spong for useful conversations regarding stability of Alfvén eigenmodes.

Declaration of interests

The work of M.L. and W.D. was performed as consultants and was not part of the employees' responsibilities to the University of Maryland. The work of J.V. was performed as a consultant and was not part of the employee's responsibilities at the University of Texas.

REFERENCES

- ALBERT, C. G., KASILOV, S. V. & KERNBICHLER, W. 2020 Accelerated methods for direct computation of fusion alpha particle losses within, stellarator optimization. *Journal of Plasma Physics* **86** (2), 815860201.
- ALONSO, J. A., CALVO, I., CARRALERO, D., VELASCO, J. L., GARCÍA-REGAÑA, J. M., PALERMO, I. & RAPIARDA, D. 2022 Physics design point of high-field stellarator reactors. *Nuclear Fusion* **62**, 036024.
- ARBEITER, F., CHEN, Y., GHIDERSA, B.-E., KLEIN, C., NEUBERGER, H., RUCK, S., SCHLINDWEIN, G., SCHWAB, F. & VON DER WETH, A. 2017 Options for a high heat flux enabled helium cooled first wall for DEMO. *Fusion Engineering and Design* **119**, 22–28.
- BADER, A., ANDERSON, D. T., DREVLAK, M., FABER, B. J., HEGNA, C. C., HENNEBERG, S., LANDREMAN, M., SCHMITT, J. C., SUZUKI, Y. & WARE, A. 2021 Modeling of energetic particle transport in optimized stellarators. *Nuclear Fusion* **61**, 116060.
- BADER, A., DREVLAK, M., ANDERSON, D. T., FABER, B. J., HEGNA, C. C., LIKIN, K. M., SCHMITT, J. C. & TALMADGE, J. N. 2019 Stellarator equilibria with reactor relevant energetic particle losses. *Journal of Plasma Physics* **85** (5), 905850508.
- BOSCH, H.-S. & HALE, G. M. 1992 Improved formulas for fusion cross-sections and thermal reactivities. *Nuclear Fusion* **32**, 611.
- CAPPA, Á., VARELA, J., BRUNA, D. LÓPEZ, ASCASÍBAR, E., LINIERS, M., ELISEEV, L.G., FONTDECABA, J.M., GARCÍA-REGAÑA, J.M., GONZÁLEZ-JEREZ, A., KHARCHEV, N.K., MEDINA, F., MELNIKOV, A.V., MULAS, S., OCHANDO, M., SPONG, D., VELASCO, J.L. & TEAM, TJ-II 2021 Stability analysis of TJ-II stellarator NBI driven Alfvén eigenmodes in ECRH and ECCD experiments. *Nuclear Fusion* **61** (6), 066019.
- CARBAJAL, L., DEL CASTILLO-NEGRETE, D., SPONG, D., SEAL, S. & BAYLOR, L. 2017 Space dependent, full orbit effects on runaway electron dynamics in tokamak plasmas. *Physics of Plasmas* **24**, 042512.
- CARBAJAL, L. & DEL-CASTILLO-NEGRETE, D. 2017 On the synchrotron emission in kinetic simulations of runaway electrons in magnetic confinement fusion plasmas. *Plasma Physics and Controlled Fusion* **59**, 124001.
- CIANCIOSA, M. 2024 BMW. <https://github.com/ORNL-Fusion/BMW>.

- DEL-CASTILLO-NEGRETE, D., CARBAJAL, L., SPONG, D. & IZZO, V. 2018 Numerical simulation of runaway electrons: 3-D effects on synchrotron radiation and impurity-based runaway current dissipation. *Physics of Plasmas* **25**, 056104.
- DEWAR, R. L. & HUDSON, S. R. 1998 Stellarator symmetry. *Physica D:Nonlinear Phenomena* **112**, 275–280.
- EL-GUEBALY, L. A. 2018 Nuclear assessment to support ARIES power plants and next-step facilities: Emerging challenges and lessons learned. *Fusion Science and Technology* **74**, 340–369.
- ELISEEV, L. G., MELNIKOV, A. V., ASCASIBAR, E., CAPPÀ, A., DRABINSKIY, M., HIDALGO, C., KHABANOV, P. O., KHARCHEV, N. K., KOZACHEK, A. S., LINIERS, M., LYSENKO, S. E., OCHANDO, M., PABLOS, J. L. DE, PASTOR, I., SHARAPOV, S. E., SPONG, D. A., BREIZMAN, B. N. & VARELA, J. 2021 Experimental observation of the geodesic acoustic frequency limit for the NBI-driven Alfvén eigenmodes in TJ-II. *Physics of Plasmas* **28** (7), 072510.
- FITZGERALD, M., DUMONT, R., KEELING, D., MAILLOUX, J., SHARAPOV, S., DREVAL, M., FIGUEIREDO, A., COELHO, R., FERREIRA, J., RODRIGUES, P., NABAIS, F., BORBA, D., ŠTANČAR, I., SZEPESI, G., TINGUELY, R. A., PUGLIA, P. G., OLIVER, H. J. C., KIPTILY, V., BARUZZO, M., LENNHOLM, M., SIREN, P., GARCIA, J. & MAGGI, C. F. 2023 Stability analysis of alpha driven toroidal Alfvén eigenmodes observed in JET deuterium-tritium internal transport barrier plasmas. *Nuclear Fusion* **63**, 112006.
- FRERICHS, H. 2024 FLARE: field line analysis and reconstruction for 3D boundary plasma modeling. *Nuclear Fusion* **64**, 106034.
- GARCIA, JERONIMO, KAZAKOV, YEVGEN, COELHO, RUI, DREVAL, MYKOLA, DE LA LUNA, ELENA, SOLANO, EMILIA R., ŠTANČAR, ŽIGA, VARELA, JACOBO, BARUZZO, MATTEO, BELLI, EMILY, BONOFIĞLO, PHILLIP J., CANDY, JEFF, MAGGI, COSTANZA F., MAILLOUX, JOELLE, MAZZI, SAMUELE, ONGENA, JEF, RUIZ, JUAN R., PORADZINSKI, MICHAL, SHARAPOV, SERGEI, ZARZOSO, DAVID & JET CONTRIBUTORS 2024 Stable Deuterium-Tritium plasmas with improved confinement in the presence of energetic-ion instabilities. *Nature Communications* **15** (1), 7846.
- GHAJ, Y., SPONG, D.A., VARELA, J., GARCIA, L., VAN ZEELAND, M.A. & AUSTIN, M.E. 2021 Effects of negative triangularity shaping on energetic particle driven Alfvén eigenmodes in DIII-D. *Nuclear Fusion* **61** (12), 126020.
- GOODMAN, A. G., XANTHOPOULOS, P., PLUNK, G. G., SMITH, H., NÜHRENBERG, C., BEIDLER, C. D., HENNEBERG, S. A., ROBERG-CLARK, G., DREVLAK, M. & HELANDER, P. 2024 Quasi-isodynamic stellarators with low turbulence as fusion reactor candidates. *PRX Energy* **3**, 023010.
- GUTTENFELDER, W. & OTHERS 2025 Predictions of core plasma performance for the infinity two fusion pilot plant. *Journal of Plasma Physics* **xx**, xx.
- HAWRYLUK, R. J., ADLER, H., ALLING, P., ANCHER, C., ANDERSON, H., ANDERSON, J. L., ASHCROFT, D., BARNES, CRIS W., BARNES, G., BATHA, S., BELL, M. G., BELL, R., BITTER, M., BLANCHARD, W., BRETZ, N. L., BUDNY, R., BUSH, C. E., CAMP, R., CAORLIN, M., CAUFFMAN, S., CHANG, Z., CHENG, C. Z., COLLINS, J., COWARD, G., DARROW, D. S., DELOOPER, J., DUONG, H., DUDEK, L., DURST, R., EFTHIMION, P. C., ERNST, D., FISHER, R., FONCK, R. J., FREDRICKSON, E., FROMM, N., FU, G. Y., FURTH, H. P., GENTILE, C., GORELENKOV, N., GREK, B., GRISHAM, L. R., HAMMETT, G., HANSON, G. R., HEIDBRINK, W., HERRMANN, H. W., HILL, K. W., HOSEA, J., HSUAN, H., JANOS, A., JASSBY, D. L., JOBS, F. C., JOHNSON, D. W., JOHNSON, L. C., KAMPERSCHROER, J., KUGEL, H., LAM, N. T., LAMARCHE, P. H., LOUGHLIN, M. J., LEBLANC, B., LEONARD, M., LEVINTON, F. M., MACHUZAK, J., MANSFIELD, D. K., MARTIN, A., MAZZUCATO, E., MAJESKI, R., MARMAR, E., MCCHESENEY, J., MCCORMACK, B., MCCUNE, D. C., MCGUIRE, K. M., MCKEE, G., MEADE, D. M., MEDLEY, S. S., MIKKELSEN, D. R., MUELLER, D., MURAKAMI, M., NAGY, A., NAZIKIAN, R., NEWMAN, R., NEWMAN, R., NISHITANI, T., NORRIS, M., O'CONNOR, T., OLDAKER, M., OSAKABE, M., OWENS, D. K., PARK, H., PARK, W., PAUL, S. F., PEARSON, G., PERRY, E., PETROV, M., PHILLIPS, C. K., PITCHER, S., RAMSEY, A., RASMUSSEN, D. A., REDI, M. H., ROBERTS, D., ROGERS, J., ROSSMASSLER, R., ROQUEMORE, A. L., RUSKOV, E., SABBAGH, S. A., SASAO, M., SCHILLING, G., SCHIVELL, J., SCHMIDT, G. L., SCOTT, S. D., SISSINGH, R., SKINNER, C. H., SNIPES,

- J., STEVENS, J., STEVENSON, T., STRATTON, B. C., STRACHAN, J. D., SYNAKOWSKI, E., TANG, W., TAYLOR, G., TERRY, J. L., THOMPSON, M. E., TUSZEWSKI, M., VANNOY, C., VON HALLE, A., VON GOELER, S., VOORHEES, D., WALTERS, R. T., WIELAND, R., WILGEN, J. B., WILLIAMS, M., WILSON, J. R., WONG, K. L., WURDEN, G. A., YAMADA, M., YOUNG, K. M., ZARNSTORFF, M. C. & ZWEBEN, S. J. 1994 Confinement and heating of a deuterium-tritium plasma. *Phys. Rev. Lett.* **72**, 3530–3533.
- HEGNA, C. C. & OTHERS 2025 The infinity two fusion pilot plant baseline plasma physics design. *Journal of Plasma Physics* **xx**, xx.
- HEIDBRINK, W. W. 2008 Basic physics of Alfvén instabilities driven by energetic particles in toroidally confined plasmas. *Physics of Plasmas* **15**, 1–15.
- HEIKKINEN, J. A., KIVINIEMI, T. P., KURKI-SUONIO, T., PEETERS, A. G. & SIPILÄ, S. K. 2001 Particle simulation of the neoclassical plasmas. *Journal of Computational Physics* **173**, 527–548.
- HEIKKINEN, J. A., KIVINIEMI, T. P., PEETERS, A. G., KURKI-SUONIO, T., SIPILÄ, S. K., HERRMANN, W., SUTTROP, W. & ZOHM, H. 1998 Ion orbit loss current in ASDEX Upgrade. *Plasma Physics and Controlled Fusion* **40**, 693–696.
- HELANDER, P. 2014 Theory of plasma confinement in non-axisymmetric magnetic fields. *Rep. Prog. Phys.* **77**, 087001.
- HIRSHMAN, S. P., VAN RIJ, W. I. & MERKEL, P. 1986 Three-dimensional free boundary calculations using a spectral Green's function method.
- HUANG, J., GAROFALO, A.M., QIAN, J.P., GONG, X.Z., DING, S.Y., VARELA, J., CHEN, J.L., GUO, W.F., LI, K., WU, M.Q., PAN, C.K., REN, Q., ZHANG, B., LAO, L.L., HOLCOMB, C.T., MCCLENAGHAN, J., WEISBERG, D., CHAN, V., HYATT, A., HU, W.H., LI, G.Q., FERRON, J., MCKEE, G., PINSKER, R.I., RHODES, T., STAEBLER, G.M., SPONG, D. & YAN, Z. 2020 Progress in extending high poloidal beta scenarios on DIII-D towards a steady-state fusion reactor and impact of energetic particles. *Nuclear Fusion* **60** (12), 126007.
- HYNÖNEN, V., KURKI-SUONIO, T., SUTTROP, W., DUX, R. & SUGIYAMA, K. 2007 Surface loads and edge fast ion distribution for co- and counter-injection in ASDEX Upgrade. *Plasma Physics and Controlled Fusion* **49**, 151–174.
- KILLER, C., GRULKE, O., DREWS, P., GAO, Y., JAKUBOWSKI, M., KNIPE, A., NICOLAI, D., NIEMANN, H., SITJES, A. PUIG & SATHEESWARAN, G. 2019 Characterization of the W7-X scrape-off layer using reciprocating probes. *Nuclear Fusion* **59**, 086013.
- KIPTILY, V. G., DUMONT, R., FITZGERALD, M., KEELING, D., SHARAPOV, S. E., PORADZINSKI, M., STANCAR, BONFIGLIO, P. J., DELABIE, E., GHANI, Z., GOLOBORODKO, V., MENMUIR, S., KOWALSKA-STRZECIWIŁK, E., PODESTÀ, M., SUN, H., TAYLOR, D. M., BERNARDO, J., CARVALHO, I. S., DOUAI, D., GARCIA, J., LENNHOLM, M., MAGGI, C. F., MAILLOUX, J., RIMINI, F. & SIREN, P. 2023 Evidence of electron heating by alpha particles in JET deuterium-tritium plasmas. *Physical Review Letters* **131**, 075101.
- KRASILNIKOV, A.V., SASAO, M., ISOBE, M., KUMAZAWA, R., MUTOH, T., TAKEIRI, Y., WATARI, T., HARTMAN, D.A., MURAKAMI, S., ALEKSEEV, A.G., AMOSOV, V.N., KASCHUCK, YU.A., PORTNOV, D.V., SAITO, K., SEKI, T., KANEKO, O., TORII, Y., IIZUKA, S., OSAKABE, M., GOTO, M., YAMADA, H., NARIHARA, K., OHYABU, N., MOTOJIMA, O. & THE LHD EXPERIMENTAL GROUP 2002 Study of acceleration and confinement of high-energy protons during ICRF and NBI heating in LHD using a natural diamond detector. *Nuclear Fusion* **42** (6), 759.
- KRIETE, D. M., PANDEY, A., PERSEO, V., SCHMITT, J. C., ENNIS, D. A., GRADIC, D., HAMMOND, K. C., JAKUBOWSKI, M., KILLER, C., KÖNIG, R., MAURER, D. A., REIMOLD, F., WINTERS, V., BEURSKENS, M. N.A., BOZHENKOV, S. A., BRUNNER, K. J., FUCHERT, G., KNAUER, J., PASCH, E. & SCOTT, E. R. 2023 Effects of drifts on scrape-off layer transport in W7-X. *Nuclear Fusion* **63**, 026022.
- KURKI-SUONIO, T., ASUNTA, O., HELLSTEN, T., HYNÖNEN, V., JOHNSON, T., KOSKELA, T., LÖNNROTH, J., PARAIL, V., ROCCELLA, M., SAIBENE, G., SALMI, A. & SIPILÄ, S. 2009 ASCOT simulations of fast ion power loads to the plasma-facing components in ITER. *Nuclear Fusion* **49**, 095001.
- KURKI-SUONIO, T., KIVINIEMI, T. P., SIPILÄ, S. K., HEIKKINEN, J. A., FUNDAMENSKI,

- W., MATTHEWS, G. F. & RICCARDO, V. 2002 Monte carlo simulations of the heat load asymmetries on JET divertor plates. *Nuclear Fusion* **42**, 725–732.
- KURKI-SUONIO, T., SARKIMAKI, K., AKASLOMPOLO, S., VARJE, J., LIU, Y., SIPILA, S., ASUNTA, O., HIRVIJOKI, E., SNICKER, A., TERAVA, J., CAVINATO, M., GAGLIARDI, M., PARAIL, V. & SAIBENE, G. 2017 Protecting ITER walls: Fast ion power loads in 3D magnetic field. *Plasma Physics and Controlled Fusion* **59**, 014013.
- LANDREMAN, M. 2017 An improved current potential method for fast computation of stellarator coil shapes. *Nuclear Fusion* **57** (4), 046003.
- LANDREMAN, M., BULLER, S. & DREVLAK, M. 2022 Optimization of quasi-symmetric stellarators with self-consistent bootstrap current and energetic particle confinement. *Physics of Plasmas* **29** (8), 082501.
- LAZERSON, A. A., KULLA, D., HARTMANN, D. A., MCNEELY, P. & RUST, N. 2023 Gyro orbit simulations of neutral beam injection in Wendelstein 7-X. *Nuclear Fusion* **63**, 096012.
- LAZERSON, S. A., FORD, O., ĀKASLOMPOLO, S., BOZHENKOV, S., SLABY, C., VAÑO, L., SPANIER, A., MCNEELY, P., RUST, N., HARTMANN, D., POLOSKEI, P., BUTTENSCHÖN, B., BURHENN, R., TAMURA, N., BUSSIAHN, R., WEGNER, T., DREVLAK, M., TURKIN, Y., OGAWA, K., KNAUER, J., BRUNNER, K. J., PASCH, E., BEURSKENS, M., DAMM, H., FUCHERT, G., NELDE, P., SCOTT, E., PABLANT, N., LANGENBERG, A., TRAVERSO, P., VALSON, P., HERGENHAHN, U., PAVONE, A., RAHBARNIA, K., ANDREEVA, T., SCHILLING, J., BRANDT, C., NEUNER, U., THOMSEN, H., CHAUDHARY, N., HÖFEL, U., STANGE, T., WEIR, G., MARUSHCHENKO, N., JAKUBOWSKI, M., ALI, A., GAO, Y., NIEMANN, H., SITJES, A. PUIG, KOENIG, R., SCHROEDER, R., HARDER, N. DEN, HEINEMANN, B., HOPF, C., RIEDL, R. & WOLF, R. C. 2021a First neutral beam experiments on Wendelstein 7-X. *Nuclear Fusion* **61**, 096008.
- LAZERSON, S. A., GEIGER, J., KULLA, D., LEVINESS, A., BOZHENKOV, S., KILLER, C., OGAWA, K., ISOBE, M., MCNEELY, P., RUST, N. & HARTMANN, D. 2024 Fast ion confinement in the presence of core magnetic islands in Wendelstein 7-X. *Plasma Physics and Controlled Fusion* **66**, 075017.
- LAZERSON, SAMUEL A., LEVINESS, ALEXANDRA & LION, JORRIT 2021b Simulating fusion alpha heating in a stellarator reactor. *Plasma Physics and Controlled Fusion* **63**, 125033.
- LAZERSON, S. A., PFEFFERLE, S., DREVLAK, M., SMITH, H., GEIGER, J., ĀKASLOMPOLO, S., XANTHOPOULOS, P., DINKLAGE, A., FORD, O., MCNEELY, P., RUST, N., BOZHENKOV, S., HARTMANN, D., RAHBARNIA, K., ANDREEVA, T., SCHILLING, J., BRANDT, C., NEUNER, U., THOMSEN, H. & WOLF, R. C. 2021c Modeling and measurement of energetic particle slowing down in Wendelstein 7-X. *Nuclear Fusion* **61**, 096005.
- MARTINELL, J. J & CARBAJAL, L. 2022 Confinement of fast ions and FLR effects in presence of magnetic islands. In *EPS*.
- MAU, T. K., KAISER, T. B., GROSSMAN, A. A., RAFFRAY, A. R., WANG, X. R., LYON, J. F., MAINGI, R., KU, L. P. & ZARNSTORFF, M. C. 2008 Divertor configuration and heat load studies for the ARIES-CS fusion power plant. *Fusion Science and Technology* **54**, 771–786.
- MOSEEV, D., ZANINI, M., KASAHARA, H., LAQUA, H., FUNABA, H., HAYASHI, W., HEIDBRINK, W., IDA, K., IGAMI, H., KAWAMOTO, Y., KENMOCHI, N., LAZERSON, S., NISHIURA, M., OCHOUKOV, R., OGAWA, K., RUD, M., SALEWSKI, M., SEKI, T., TAMURA, N., TANAKA, K., TOKUZAWA, T. & YOSHINUMA, M. 2024 Influence of sawtooth oscillations on fast ions in a stellarator. *Nuclear Fusion* **64**, 066028.
- NEMOV, V. V., KASILOV, S. V., KERNBICHLER, W. & LEITOLD, G. O. 2008 Poloidal motion of trapped particle orbits in real-space coordinates. *Physics of plasmas* **15** (5), 052501.
- NORAJITRA, P., BASUKI, W. W., GINIYATULIN, R., HERNANDEZ, C., KUZNETSOV, V., MAZOUZ, I. V., RICHOU, M. & SPATAFORA, L. 2015 Recent Progress in the Development of Helium-Cooled Divertor for DEMO. *Fusion Science and Technology* **67** (4), 732–744, arXiv: <https://doi.org/10.13182/FST14-832>.
- OGAWA, K., ISOBE, M., SANGAROON, S., LIAO, L. Y., ZHONG, G. Q., SEKI, R., NUGA, H. & OSAKABE, M. 2024 Observation of energetic ion anisotropy using neutron diagnostics in the large helical device. *Nuclear Fusion* **64**, 076010.
- OGAWA, K., ISOBE, M., TOI, K., SHIMIZU, A., SPONG, D. A., OSAKABE, M. & YAMAMOTO, S. 2013 A study on the TAE-induced fast-ion loss process in LHD. *Nuclear Fusion* **53**, 053012.

- OGAWA, K., ISOBE, M., TOI, K., WATANABE, F., SPONG, D.A., SHIMIZU, A., OSAKABE, M., OHDACHI, S., SAKAKIBARA, S. & GROUP, LHD EXPERIMENT 2010 Observation of energetic-ion losses induced by various mhd instabilities in the large helical device LHD. *Nuclear Fusion* **50** (8), 084005.
- PACE, D. C., AUSTIN, M. E., BARDOCZI, L., COLLINS, C. S., CROWLEY, B., DAVIS, E., DU, X., FERRON, J., GRIERSON, B. A., HEIDBRINK, W. W., HOLCOMB, C. T., MCKEE, G. R., PAWLEY, C., PETTY, C. C., PODESTÀ, M., RAUCH, J., SCOVILLE, J. T., SPONG, D. A., THOME, K. E., VAN ZEELAND, M. A., VARELA, J. & VICTOR, B. 2018 Dynamic neutral beam current and voltage control to improve beam efficacy in tokamaks. *Physics of Plasmas* **25** (5), 056109.
- PAUL, E. J., BHATTACHARJEE, A., LANDREMAN, M., ALEX, D., VELASCO, J. L. & NIES, R. 2022 Energetic particle loss mechanisms in reactor-scale equilibria close to quasisymmetry. *Nuclear Fusion* **62**, 126054.
- PAUL, E. J., MYNICK, H. E. & BHATTACHARJEE, A. 2023 Fast-ion transport in quasisymmetric equilibria in the presence of a resonant Alfvénic perturbation. *Journal of Plasma Physics* **89**.
- PAZ-SOLDAN, C., EIDIETIS, N. W., HOLLMANN, E. M., ALEYNIKOV, P., CARBAJAL, L., HEIDBRINK, W. W., HOPPE, M., LIU, C., LVOVSKIY, A., SHIRAKI, D., SPONG, D., BRENNAN, D. P., COOPER, C. M., DEL-CASTILLO-NEGRETE, D., DU, X., EMBREUS, O., FULOP, T., HERFINDAL, J., MOYER, R., PARKS, P. & THOME, K. E. 2019 Recent DIII-D advances in runaway electron measurement and model validation. *Nuclear Fusion* **59**, 066025.
- PROST, V. & VOLPE, F. A. 2023 Economically optimized design point of high-field stellarator power-plant. *Nuclear Fusion* p. 026007.
- SÁNCHEZ, E., VELASCO, J. L., CALVO, I. & MULAS, S. 2023 A quasi-isodynamic configuration with good confinement of fast ions at low plasma β . *Nuclear Fusion* **63** (6), 066037.
- SCOTT, S. D., KRAMER, G. J., TOLMAN, E. A., SNICKER, A., VARJE, J., SÄRKIMÄKI, K., WRIGHT, J. C. & RODRIGUEZ-FERNANDEZ, P. 2020 Fast-ion physics in SPARC. *Journal of Plasma Physics* **86**, 865860508.
- SHINOHARA, K., KURKI-SUONIO, T., SPONG, D., ASUNTA, O., TANI, K., STRUMBERGER, E., BRIGUGLIO, S., KOSKELA, T., VLAD, G., GÜNTER, S., KRAMER, G., PUTVINSKI, S. & HAMAMATSU, K. 2011 Effects of complex symmetry-breakings on alpha particle power loads on first wall structures and equilibrium in ITER. *Nuclear Fusion* **51**, 063028.
- SNICKER, A., SIPILÄ, S. & KURKI-SUONIO, T. 2012 Orbit-following fusion alpha wall load simulation for iter scenario 4 including full orbit effects. *Nuclear Fusion* **52**, 094011.
- SPONG, D.A., VAN ZEELAND, M.A., HEIDBRINK, W.W., DU, X., VARELA, J., GARCIA, L. & GHAI, Y. 2021 Nonlinear dynamics and transport driven by energetic particle instabilities using a gyro-Landau closure model. *Nuclear Fusion* **61** (11), 116061.
- SPONG, D. A. 2013 Simulation of Alfvén frequency cascade modes in reversed shear-discharges using a Landau-closure model. *Nuclear Fusion* **53** (5), 053008.
- SPONG, D. A., D'AZEVEDO, E. & TODO, Y. 2010 Clustered frequency analysis of shear Alfvén modes in stellarators. *Physics of Plasmas* **17**, 022106.
- SPONG, D. A., SANCHEZ, R. & WELLER, A. 2003 Shear Alfvén continua in stellarators. *Physics of Plasmas* **10**, 3217–3224.
- SUN, Y.X., HUANG, J., GONG, X.Z., GAROFALO, A.M., SALEWSKI, M., VARELA, J., QIAN, J.P., ZHANG, X.J., FAN, T.S., WANG, J.F., ZHANG, W., HAO, B.L., GAO, W., CHANG, J.F., ZHONG, G.Q., ZANG, Q., LIU, H.Q., LYU, B., XIE, Y.H. & WANG, X.H. 2024 Fast ion studies in the extended high-performance high β_P plasma on EAST. *Nuclear Fusion* **65** (1), 016040.
- SÄRKIMÄKI, KONSTA 2019 Modelling and understanding fast particle transport in non-axisymmetric tokamak plasmas. PhD thesis, Aalto University.
- TAIMOURZADEH, S., BASS, E.M., CHEN, Y., COLLINS, C., GORELENKOV, N.N., KÖNIES, A., LU, Z.X., SPONG, D.A., TODO, Y., AUSTIN, M.E., BAO, J., BIANCALANI, A., BORCHARDT, M., BOTTINO, A., HEIDBRINK, W.W., KLEIBER, R., LIN, Z., MISHCHENKO, A., SHI, L., VARELA, J., WALTZ, R.E., YU, G., ZHANG, W.L. & ZHU, Y. 2019 Verification and validation of integrated simulation of energetic particles in fusion plasmas. *Nuclear Fusion* **59** (6), 066006.
- VARELA, J., COOPER, W.A., NAGAOKA, K., WATANABE, K.Y., SPONG, D.A., GARCIA, L.,

- CAPPA, A. & AZEGAMI, A. 2020a Effect of the tangential NBI current drive on the stability of pressure and energetic particle driven MHD modes in LHD plasma. *Nuclear Fusion* **60** (2), 026016.
- VARELA, J., HIDALGO, C., TOKUZAWA, T., NAGAOKA, K., TANAKA, K., NAGASAKI, K., OHDACHI, S., IDA, K., DU, X., CAPPA, A., SHARAPOV, S., ZARZOSO, D., SPONG, D.A., GARCIA, L., GHAI, Y. & ORTIZ, J. 2024a Generation of shear flows induced by AE / EPM in LHD plasma. *Nuclear Fusion* **65** (2), 026002.
- VARELA, J., NAGAOKA, K., TAKEMURA, Y., WATANABE, K. Y., IDA, K., YOSHINUMA, M., NAGASAKI, K., CAPPA, A., SHARAPOV, S., SPONG, D. A., GARCIA, L., GHAI, Y. & ORTIZ, J. 2024b MHD stability trends and improved performance of LHD inward-shifted configurations: The role of the neutral beam current drive and thermal plasma density. *Physics of Plasmas* **31** (8), 082504.
- VARELA, J., NAGAOKA, K., TAKEMURA, Y., WATANABE, K. Y., IDA, K., YOSHINUMA, M., NAGASAKI, K., CAPPA, A., SHARAPOV, S., SPONG, D. A., GARCIA, L., GHAI, Y. & ORTIZ, J. 2024c MHD stability trends and improved performance of LHD inward-shifted configurations: The role of the neutral beam current drive and thermal plasma density. *Physics of Plasmas* **31** (8), 082504.
- VARELA, J., NAGASAKI, K., KOBAYASHI, S., NAGAOKA, K., ADULSIRISWAD, P., CAPPA, A., YAMAMOTO, S., WATANABE, K.Y., SPONG, D.A., GARCIA, L., GHAI, Y. & ORTIZ, J. 2022a Analysis of the ECH effect on EPM/AE stability in Heliotron J plasma using a Landau closure model. *Nuclear Fusion* **63** (2), 026009.
- VARELA, J., NAGASAKI, K., NAGAOKA, K., YAMAMOTO, S., WATANABE, K. Y., SPONG, D. A., GARCIA, L., CAPPA, A. & AZEGAMI, A. 2020b Modeling of the ECCD injection effect on the Heliotron J and LHD plasma stability. *Nuclear Fusion* **60** (11), 112015.
- VARELA, J., SPONG, D.A. & GARCIA, L. 2017a Analysis of Alfvén eigenmodes destabilization by energetic particles in TJ-II using a Landau-closure model. *Nuclear Fusion* **57** (12), 126019.
- VARELA, J., SPONG, D.A. & GARCIA, L. 2017b Analysis of Alfvén eigenmode destabilization by energetic particles in Large Helical Device using a Landau-closure model. *Nuclear Fusion* **57** (4), 046018.
- VARELA, J., SPONG, D., GARCIA, L., GHAI, Y. & ORTIZ, J. 2024d Stability optimization of energetic particle driven modes in nuclear fusion devices: the FAR3d gyro-fluid code. *Frontiers in Physics* **12**.
- VARELA, J., SPONG, D.A., GARCIA, L., HUANG, J., MURAKAMI, M., GAROFALO, A.M., QIAN, J.P., HOLCOMB, C.T., HYATT, A.W., FERRON, J.R., COLLINS, C.S., REN, Q.L., MCCLENAGHAN, J. & GUO, W. 2018 Analysis of Alfvén eigenmode destabilization in DIII-D high poloidal β discharges using a Landau closure model. *Nuclear Fusion* **58** (7), 076017.
- VARELA, J., SPONG, D.A., GARCIA, L., OHDACHI, S., WATANABE, K.Y. & SEKI, R. 2019a Analysis of the MHD stability and energetic particles effects on EIC events in LHD plasma using a Landau-closure model. *Nuclear Fusion* **59** (4), 046008.
- VARELA, J., SPONG, D.A., GARCIA, L., OHDACHI, S., WATANABE, K.Y., SEKI, R. & GHAI, Y. 2021 Theoretical analysis of the saturation phase of the 1/1 energetic-ion-driven resistive interchange mode. *Nuclear Fusion* **61** (12), 126016.
- VARELA, J., SPONG, D.A., MURAKAMI, M., GARCIA, L., D'AZEVEDO, E., VAN ZEELAND, M.A. & MUNARETTO, S. 2019b Subdominant modes and optimization trends of DIII-D reverse magnetic shear configurations. *Nuclear Fusion* **59** (4), 046017.
- VARELA, J., SPONG, D.A., TODO, Y., GARCIA, L., GHAI, Y., ORTIZ, J. & SEKI, R. 2022b Simulation of the TAEs' saturation phase in the Large Helical Device: MHD burst. *Nuclear Fusion* **62** (12), 126020.
- VAY, J. 2008 Simulation of beams or plasmas crossing at relativistic velocity. *Physics of Plasmas* **15**, 056701.
- VELASCO, J. L., CALVO, I., MULAS, S., SÁNCHEZ, E., PARRA, F. I., CAPPA, A. & OTHERS 2021 A model for the fast evaluation of prompt losses of energetic ions in stellarators. *Nuclear Fusion* **61** (11), 116059.
- WANG, X.H., HUANG, J., VARELA, J., ZHAO, H.L., SPONG, D.A., XU, L.Q., SHEN, W., CHANG, J.F., FU, J., SUN, Y.X., SHI, C., WANG, S.S. & THE EAST TEAM

- 2023 Analysis of beam ion driven Alfvén eigenmode stability induced by Tungsten contamination in EAST. *Nuclear Fusion* **64** (1), 016028.
- WARMER, F., BEIDLER, C. D., DINKLAGE, A. & WOLF, R. 2016 From W7-X to a HELIAS fusion power plant: Motivation and options for an intermediate-step burning-plasma stellarator. *Plasma Physics and Controlled Fusion* **58**, 074006.
- YAMAMOTO, S., NAGASAKI, K., NAGAOKA, K., VARELA, J., CAPP, Á., ASCASÍBAR, E., CASTEJÓN, F., FONTDECABA, J.M., GARCÍA-REGAÑA, J.M., GONZÁLEZ-JEREZ, Á., IDA, K., ISHIZAWA, A., ISOBE, M., KADO, S., KOBAYASHI, S., LINIERS, M., LÓPEZ-BRUNA, D., MARUSHCHENKO, N., MEDINA, F., MELNIKOV, A., MINAMI, T., MIZUUCHI, T., NAKAMURA, Y., OCHANDO, M., OGAWA, K., OHSHIMA, S., OKADA, H., OSAKABE, M., SANDERS, M., VELASCO, J.L., WEIR, G. M. & YOSHINUMA, M. 2020 Effect of ECH/ECCD on energetic-particle-driven MHD modes in helical plasmas. *Nuclear Fusion* **60** (6), 066018.
- ZHANG, RUILI, LIU, JIAN, QIN, HONG, WANG, YULEI, HE, YANG & SUN, YAJUAN 2015 Volume-preserving algorithm for secular relativistic dynamics of charged particles. *Physics of Plasmas* **22**, 044501.
- ÄKÄSLOMPOLO, S., DREVLAK, M., TURKIN, Y., BOZHENKOV, S., JESCHE, T., KONTULA, J., KURKI-SUONIO, T., WOLF, R. C. & W7-X TEAM 2018 Modelling of NBI ion wall loads in the W7-X stellarator. *Nuclear Fusion* **58**, 082010.